Human Mesenchymal Stem Cell Behaviour on Meso-Scale Substrate Curvature:

A Finite Element Analysis of the Effects of Substrate Curvature on Cellular Traction Forces and Morphology

A.S. Tjernshaugen

Master of Science Thesis

TU Delft
Delft University of Technology

MSc Biomedical Engineering

Human Mesenchymal Stem Cell Behaviour on Meso-Scale Substrate Curvature:

A Finite Element Analysis of the Effects of Substrate Curvature on Cellular Traction Forces and Morphology

Master of Science Thesis

For the degree of Master of Science in Biomedical Engineering at
Delft University of Technology

A.S. Tjernshaugen

Graduation Date: August 29, 2022

Student number:	5218527
Thesis committee:	Dr.ir. N.Tumer
	Prof.dr. A.A. Zadpoor
	Dr.ir. M.P. Peirlinck
	Dr. A. Accardo
Supervisor Team:	Dr.ir E.L Fratila-Apachitei
	Dr.ir. N.Tumer

Faculty of Mechanical, Maritime, and Materials Engineering
Delft University of Technology

Abstract

That mechanical properties of the extracellular environment can influence cell behaviour has already been established. Recent studies indicate that human mesenchymal stem cells are affected by the surface curvature of the underlying substrate. However, how meso-scale substrate curvature affects cell behaviour is still not clear. This study utilised the finite element method to simulate a prestressed human mesenchymal stem cell conforming and attaching to a flat control substrate, concave hemispherical and concave cylindrical substrates with curvature radii from 300 µm to 75 µm. The cell model comprises the actin cortex, cytoskeleton, and nucleus modelled with a hyperelastic material definition and 30 linear elastic stress fibres prestressed with a force of 10 nN. The effects of surface curvature on cellular traction forces, cell height, nuclear aspect ratio and actin cortex was studied. The vertical traction forces were observed to be 70% and 40% lower for the hemispherical and cylindrical substrates of the highest curvatures compared to the flat control substrate, respectively. Cellular traction forces towards the cell periphery were roughly 10-20% higher than the more central cellular traction forces independent of substrate curvature. Stresses in the actin cortex were observed to increase by 290% and 220% from the flat control substrate to the hemispherical and cylindrical substrates of the highest curvatures, respectively. These results indicate that the cell is more sensitive to hemispherical substrates than cylindrical substrates. The results also support in vitro observations where hMSCs are seen to span hemispherical substrates and avoid continuous contact.

Table of Contents

Acknowledgements

I want to express my deepest gratitude to my supervisors, Dr.ir. N.Tumer and Dr.ir. E.L. Fratila-Apachitei for providing constant guidance and advice throughout my project. I am also grateful for the valuable input provided by Prof.dr. A.A. Zadpoor.

Delft, University of Technology A.S. Tjernshaugen

Nomenclature

$2D$	Two Dimensional
$3D$	Three Dimensional
CM	Computational Model
CSK	Cytoskeleton
CZM	Cohesive Zone Model
DOF	Degrees of Freedom
DPM	Discrete Particle Method
ECM	Extracellular Matrix
FA	Focal Adhesion
FEA	Finite Element Analysis
FEM	Finite Element Method
H	Mean Curvature
$hbMSC$	Human Bonemarrow Stromal Cell
$hMSC$	Human Mesenchymal Stem Cell
K	Gaussian Curvature
$LINC$	Linker of Nucleoskeleton and Cytoskeleton
MSC	Mesenchymal Stem Cell
SF	Stress Fibre
TFM	Traction Force Microscopy

Chapter 1

Introduction

Cells are constantly influenced by their surrounding environment; the extracellular matrix (ECM) plays a crucial role both in the preservation of the structural integrity of tissues and in generating new tissue [1–3]. Human mesenchymal stem cells (hMSCs) have been widely researched due to their ability to proliferate, and their multipotency [4]. By altering ECM properties, hMSCs may differentiate into osteoblasts, adipocytes or chondrocytes accordingly [5]. hMSCs have been observed to be particularly mechanosensitive, modulating their phenotype based on feedback from probing their external environment [6]. Cells probe their environment by forming temporary and longer-lasting adhesions to the surrounding ECM [7]. Cell-substrate adhesion represents a series of vital and complex interactions between a cell, and a substrate surface [8]. The process involves membrane proteins, cytoskeletal remodelling and cell contraction. Transmembrane proteins (integrins) cluster and recruit adhesome proteins on the inner side of the cell membrane, forming focal adhesions (FAs). Intracellularly, FAs form bonds with actin stress fibres (SF) [9]. SFs comprise long thin chains of polymerised actin molecules and myosin motor proteins and form the cytoskeletal network's tensile units [10]. The myosin motor proteins enable the SFs to contract, and in their resting state, SFs have been observed to exhibit a pre-existing prestress. These contractile forces result in tractional forces applied by the FAs to the ECM [11]. FAs are highly dynamic and grow and disassemble in response to an increase or decrease in these traction forces, respectively [12]. It has been observed that FAs can grow to sizes with diameters larger than 5 μm and often experience traction forces in the nanonewton range [13].

Some SFs also form a mechanical link to the nucleus via LINC complexes on the nuclear envelope [14]. Physical characteristics of the external environment can be directly transmitted to the nucleus as mechanical forces via the SFs [15]. These forces have been observed to alter the nuclear shape and size [6]. Dorsal and transverse stress fibres and more localised actin structures like lamellipodia and filopodia are known to modulate cell shape in response to environmental cues. The two latter structures also play an essential role in cell migration [16]. Consequently, external biophysical cues can influence the genomic structure, gene expression and cell fate by altering nuclear and cell shape [17].

Biophysical cues, such as stiffness, porosity and topography of substrates have been observed to modulate hMSC behaviour [18–20]. Engler et al. famously showed that MSCs seeded on substrates of different stiffness induced a preference for neuronal (0.1-1 kPa), myoblastic (8-17 kPa) and osteoblastic (25-40 kPa) differentiation [21]. More recently, studies show that the geometrical features of the ECM also play a crucial role in regulating cellular behaviour [22–34]. Cell behaviour influenced by 2D geometry have been widely studied. Micropatterned and nanopatterned substrates are used to investigate how various geometries affect cell shape and organisation of SF and FAs [24]. Lee et al. observed that single cells constrained to circular patterns induced less intracellular tension than single cells constrained to star and oval-shaped patterns [25]. The reduced intracellular tension resulted in the hMSC maintaining its multipotency. Another study found that elevated tensional stresses towards the corner regions of square adhesive patterns encouraged lamellipodia extensions [26]. Generally, 2D surfaces fail to capture essential aspects of the extracellular environment [17]. *In vivo*, hMSCs are surrounded by three-dimensional (3D) topographical cues like meso-scale curvature and microscale curvature in the form of grooves, ridges, and pores [35]. 3D substrates, therefore, more accurately mimic the in vivo hMSC environment. Studies investigating how 3D environments affect cell morphology and cellular behaviour such as migration, proliferation, and differentiation are still limited in numbers. Park showed that fibroblasts and MSCs actively migrated out of concave pits (diameter: 200 µm), preferring to attach and proliferate on convex structures (diameter: 300 µm) [27]. Macrophages have been found to avoid convex substrates altogether, emphasising that different cell phenotypes may respond differently to similar substrate geometries [34]. It has also been observed that the degree of curvature of 3D spherical pores influenced MSC morphology and osteogenic differentiation [31]. More recently, Werner et al. found that human bone marrow stromal cells (hbMSCs) minimised their substrate contact points in concave pits (diameter: 250 µm-750 µm) by spanning parts of the substrate [36]. The same cells were found to remain in complete contact with convex substrates and express a flattened nucleus. The type of curvature also affected the distribution of focal adhesions, with fewer FAs present in the central regions below the nucleus for the hbMSCs in the concave pits. These studies provided qualitative data to show that cell behaviour and fate are modulated by meso-scale curvature. No studies were found that obtained quantitative information of the effect of meso-scale surface curvature on hMSC behaviour and morphology. Methods such as traction force microscopy (TFM), atomic force microscopy (AFM), optical tweezers, and magnetic beads, makes it possible to measure the traction forces exerted by the cell as it adheres and migrates on substrates [37]. However, TFM is usually conducted on micropatterned surfaces, where traction forces are determined based on the magnitude of deformation that cells apply to soft micropillars [38]. TFM is not yet suited to quantify traction forces on substrates with meso-scale curvature. Moreover, producing the sufficient number of samples with the desired surface geometry, and screening the response of a sufficient number of cells to enable statistical analyses are cumbersome and costly [39]. Consequently, computational models (CM) offer a powerful complementary tool. Comprising a variety of approaches, CMs employ mathematical models to predict cell morphology and cellular behaviours like cytoskeletal arrangement, and migration [40]. However, the number of computational models investigating cellular behaviour on meso-scale substrate curvature is limited. The only model found employing the finite element method (FEM) was developed by Sanz-Herrera et al. [41]. A fibroblast was modelled as a spherical disc attached to convex cylindrical, hemispherical, and hyperbolic substrates with a curvature ranging from one to six times the diameter of the cell. Qualitatively studying the differences in stress distributions of the cell, they found that the stresses increased towards the cell periphery and away from the nucleus. Two other apply the discrete particle method (DPM) to investigate cellular behaviour on meso-scale substrate curvature [42, 43]. Employing the network approach, where membrane particles mechanically link to nucleus particles, He et al. observed that adherent cells were more sensitive to convex cylinders than concave cylinders, altering their shape at a fourfold faster speed when the radius of curvature was within the range of 20 µm - 100 µm [42]. Vassaux et al. found that the intracellular tension of hMSCs increased with the degree of convexity of hemispherical substrates (radius: 75 µm - 500 µm) using a discrete particle model (DPM) where different types of subcellular particles interact with each other according to specified interaction laws [43]. A correlation was established between increased concave curvature and increased compressive forces. Further, they observed that the nucleus experienced more significant deformations on convex substrates than on concave ones. The model was later utilised to investigate the migration pattern of hMSCs on curved substrates [44].

Nevertheless, there is a distinct lack of research on how meso-scale surface curvature affects cellular traction forces. Therefore, this thesis aims to utilise FEM to perform an exploratory study investigating how concave surfaces with different meso-scale curvatures affect traction forces and morphology of hMSCs.

Chapter 2

Methods

The computational model created in this study investigated changes in cell morphology and cellular behaviour of an hMSC conformed to concave substrates and a flat control substrates. The concave substrates included hemispherical and cylindrical surfaces with radii of curvatures, r_c, ranging from 75 μm to 300 μm. The model was developed using the finite element software Abaqus/Standard 2019 and the geometry and material properties are primarily based on the model developed by Migliorini and colleagues in 2021 [45]. Their work performed an *in silico* AFM indentation test to derive the material properties of the hMSC. *In vitro* AFM is commonly used to characterise cell mechanical properties [46]. AFM can also detach and place cells on substrates [46]. The present study simulated a situation where AFM is used to place an hMSC onto underlying substrates of different meso-scale surface curvatures. The model was validated using a flat substrate against experimental results reported by Migliorini et al. (see appendix A-0-2) [45]. Once the model was validated, several analyses with hemispherical and cylindrical surfaces of different curvatures were performed. Resultant cell traction forces and morphology were then analysed and statistically compared between the different surfaces.

2-1 Cell Geometry and Material Properties

Cells are found embodying many morphologies, and it is rare to find two cells with completely alike geometries [47]. The overall cell geometry used by Migliorini and this study attempt to capture the general hMSC morphology and dimensions [45]. Modelled as a spherically spread cell shown in Figure 2-1, the maximum height of the hMSC is 13 µm at the centre [45]. The maximum diameter at the base is 50 µm. The nucleus is represented by a solid sphere with a diameter of 10 µm and is located in the centre of the cell [45]. The actin cortex, a structure comprising a thin meshwork of F-actin fibres that underlies the cell membrane [48], was simplified to a continuous membrane of a uniform thickness of 0.2 nm surrounding the cytoskeleton (CSK) [45]. Multiple research studies have found cells to exhibit viscoelastic properties *in vitro* [49–52]. *In silico*, material properties such as viscoelasticity, poro-hyperelasticity, and hyperelasticity have been used to describe the behaviour of the cell [53–55]. Migliorini et al. utilised the hyperelastic Aruda-Boyce model [45]. Accordingly, the present work employs the same model for the cell actin cortex, CSK and nucleus.

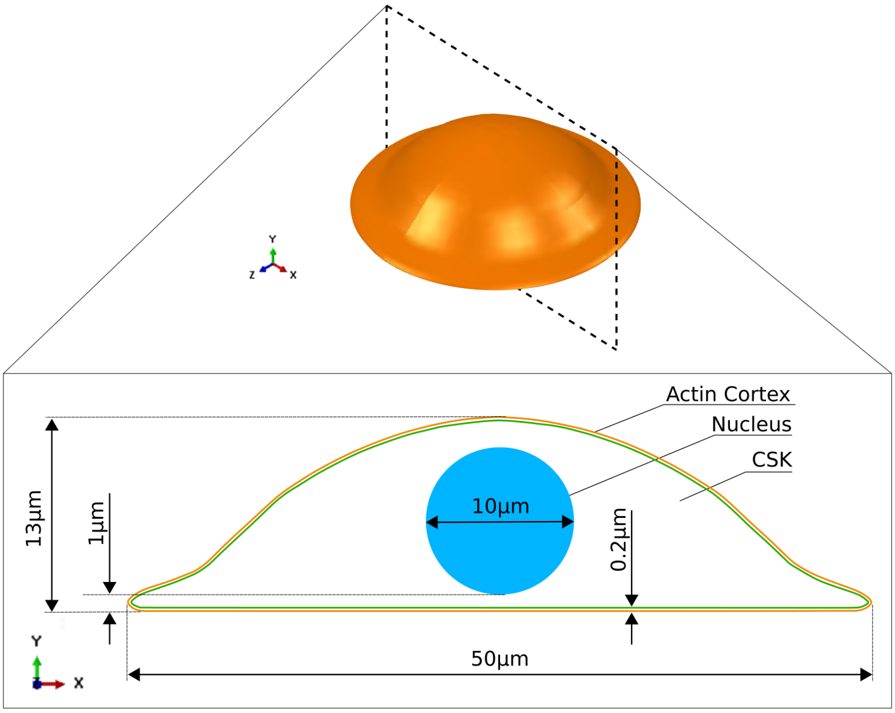

Figure 2-1: Schematic showing the overall geometry of the hMSc Cell, based on [45].

Abaqus requires three input parameters for the Arruda-Boyce model; the shear modulus ($\mu_{\text{eight-chain}}$), the distensibility (λ_L), and D. The shear modulus describes the shear stiffness of a material, while the distensibility captures the degree of stretch of the material [56]. D is a material constant related to the bulk modulus, κ, as described in Equation 2-1 [56].

$$D = \frac{\kappa}{2} \tag{2-1}$$

The bulk modulus can be derived using Equation 2-2 and Equation 2-3.

$$\kappa = \frac{E_{\text{eight-chain}}}{3(1-2v)} \tag{2-2}$$

$$E_{\text{eight-chain}} = 2(1+v)\mu_{\text{eight-chain}} \tag{2-3}$$

Where $E_{\text{eight-chain}}$ is the Young's modulus of the material, and v is the Poisson's ratio.

In this work, the average material properties calculated by Migliorini are used with values listed in Table 2-1. Densities of the nucleus and CSK are set to 1.8×10^{-9} $tonnes/mm^3$ and 1.5×10^{-9} $tonnes/mm^3$, in line with Milner et al. [57]. The density of the actin cortex was set to 8.45×10^{-8} $tonnes/mm^3$ [58].

Table 2-1: hMSC material properties for the Arruda-Boyce hyperelastic model used for the cytoskeleton, actin cortex and nucleus. [45].

Cell Properties	μ_{8chain} (Pa)	λ_L	E_{AB} (Pa)
Cytoskeleton	1198.796	3.065	3596.387
Actin Cortex	3225.798	3.083	9677.394
Nucleus	12000	3.07	35997.6

Research shows that some stress fibres are mechanically linked to the nucleus via the linker of nucleoskeleton and cytoskeleton (LINC) complexes on the nuclear lamina [15]. These features have a larger cross-sectional area and distribute the contractile forces over larger areas. Figure 2-2A shows how the stress fibres span from one end of the cell to the other and form an mechanically link to the nucleus [15]. In the study conducted by Migliorini, stress fibres trail the cell periphery and do not directly interact with the nucleus. The present study investigates how stress fibres linked to the nucleus affect nuclear morphology. As such, an approach similar to the one utilised by Milner et al. was chosen [57]. Figure 2-2C shows the employed approach, where stress fibres tether the nucleus to the actin cortex.

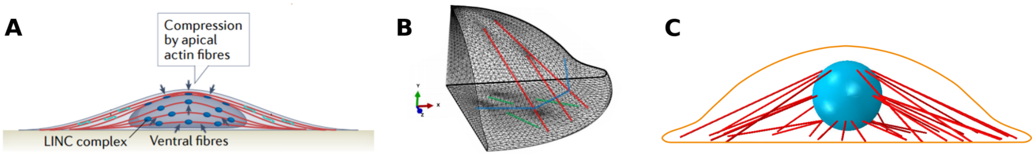

Figure 2-2: **A**: Schematic of how ventral and apical actin stress fibres surround and tether to the nuclear envelope via LINC complexes [15]. **B**: Schematic showing ventral (green), dorsal (red) and transverse (blue) stress fibres modelled by Migliorini et al. [45]. **C**: Schematic showing the simplified actin stress fibre placement used in the present model.

In line with previous work [45, 57], the SFs mod waselled as only tension-bearing trusses with a constant cross-sectional area. Geometrical and material properties are listed in Table 2-2 [45, 58]. SF prestress was achieved by applying a thermal expansion coefficient (see Table 2-2) to the stress fibre material definition. An embedded definition was used instead of tie constraints to constrain the SFs to the nucleus and actin cortex, to avoid stress fibres connecting to single nodes.

Table 2-2: Material and geometrical properties of the stress fibres (SFs) in the present model.

Properties of SF	Value	Reference
E (kPa)	330	[45]
Poisson's Ratio	0.3	[45]
Thermal Expansion Coefficient	0.005	
Density ($tonnes/mm^3$)	8.45E-08	[58]
Cross-Sectional Area (μm^2)	0.05	[45]

Like Milner et al., 30 stress fibres were generated, tethering the nucleus to the actin cortex [57]. A Matlab script was used to generate random coordinates, representing the locations where the stress fibres tether to the focal adhesions. The FA areas were randomly generated and embodied imperfect spherical shapes. The average surface area per focal adhesion was calculated to be 3.66 μm^2. This area corresponds well with literature where focal adhesions have been observed to have areas varying from 0.2 μm^2 to 5 μm^2 [59]. The FAs and corresponding SFs were divided into three groups based on the distance between the FA and the tethering location on the nucleus; distal, medial and central. The distal, medial and central groups comprised the FAs furthest away, second furthest away, and closest to the cell centre, respectively, as shown in Figure 2-3. The stress fibres' direction and length were calculated based on two criteria. Firstly, each stress fibre was angled radially towards the vertical centreline of the cell. Secondly, the distal group of SF tethered to the apical surfaces of the nucleus, while the central and medial SFs tethered to the inferior surface and medial transverse circumference, respectively. Figure 2-3 shows the resultant distribution of stress fibres and focal adhesions. The distribution is non-uniform, with a majority of SF aligning along X-axis. The average length and standard deviation of each SF group are listed in Table 2-3.

Table 2-3: Average stress fibre length and standard deviation for each SF group.

SF Group	Average Length (µm)	Standard Deviation
Distal	22.15	0.48
Medial	16.79	1.36
Central	9.20	3.82

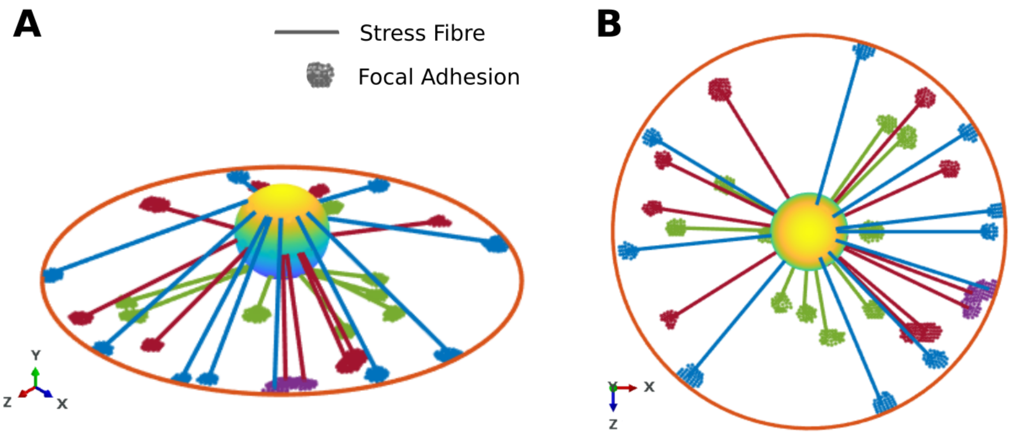

Figure 2-3: A & B: Orthogonal and top views of focal adhesion and stress fibre distribution within the hMSC model. Blue: distal group, Red: medial group, Green: central group.

2-2 Substrate Geometry and Material Properties

The type and degree of the surface curvature of the substrates were the main parameters that were varied in the present work. Surface curvature is an essential property that describes the local geometry of an object [60]. The property's locality indicates that the measured curvature varies at different surface points [61]. The terms "concavity" and "convexity" are often used for a sphere's internal and external faces, respectively. However, they cannot differentiate between different types of curvatures like cylindrical and spherical surfaces [60]. Therefore, the curvature of a substrate is often described using the Gaussian (K) and the mean (H) curvatures defined in Equation 2-4 and Equation 2-5 [62].

$$K = \kappa_1 \times \kappa_2 \tag{2-4}$$

$$H = \frac{1}{2}(\kappa_1 + \kappa_2) \tag{2-5}$$

Where κ_1 and κ_2, the principal curvatures, are the minimum and maximum values of curvatures at a given point on the surface [62]. The curvature, κ, is defined as the inverse of the radius of curvature (r_c) [60]. The radius of curvature of a point on a surface is measured as the reciprocal of the osculating circle at that point [62]. It should be noted that the radius of curvature decreases as curvature increases. Gaussian curvature is an intrinsic property of the surface [63]. As shown in Figure 2-4, a spherical shape always has a positive Gaussian curvature $(K > 0)$, regardless of whether the surface is considered convex or concave [64]. Similarly, a flat plane and a cylinder always yield zero Gaussian curvature $(K = 0)$ as at least one of the principal curvatures remains zero. A hyperbolic surface always has negative Gaussian curvature $(K < 0)$ as the principal curvatures have opposite sign conventions. Consequently, the sign convention of Gaussian curvature conveys essential information regarding the local shape [63]. The mean curvature is an extrinsic property whose sign convention depends on the defined direction of the surface normal. However, flat planes always have a zero mean curvature, while non-flat planes always have a non-zero mean curvature.

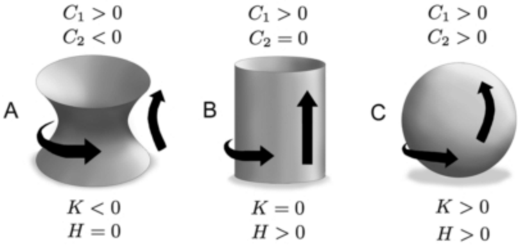

Figure 2-4: Schematic showing principal curvatures (C_1, C_2), Gaussian curvature (K) and mean curvature (H) for **A)** Saddle Shape **B)** Cylinder **C)** Sphere [64]

.

In this study, the types of surface curvatures investigated were concave hemispheres $(K > 0, H > 0)$ and concave cylinders $(K = 0, H > 0)$, as shown in Figure 2-5. The degree of curvature varied for each surface, with the corresponding values listed in Table 2-4. Substrates with surface curvatures larger than $1/75\ /mum$ $(\kappa > 1/75\ \mu m^{-1})$ were not considered as they caused convergence issues.

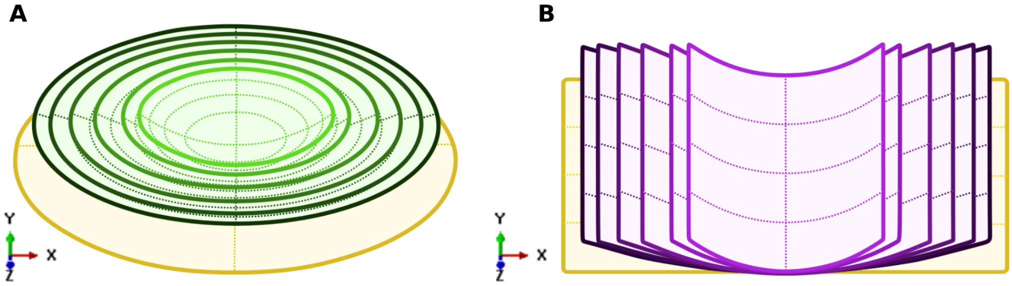

Figure 2-5: Schematic showing the types of curvatures used in simulation. The curvature varies from κ= 1/300 µm to 1/75 µm from the darkest to the lightest shade. The yellow surfaces represent the flat control surfaces. **A:** hemisphere $(K > 0,\ H > 0)$, **B:** cylinder $(K = 0,\ H > 0)$.

The substrates were modelled as rigid, analytical surfaces as they are stiffer than the cell by multiple orders of magnitude. Using a rigid material definition also reduces convergence issues and is less computationally demanding.

Table 2-4: The range of curvatures investigated for the hemispherical ($K > 0,\ H > 0$) and cylindrical substrates ($K = 0,\ H > 0$).

r_c (µm)	κ(μm^{-1})
75	1/75
100	1/100
150	1/150
200	1/200
250	1/250
300	1/300
∞ (flat)	0

2-3 Contact Definitions and Model Constraints

Contact definitions were defined between the actin cortex and the surface of the substrate. Tangential contact was defined with a penalty coefficient of 0.2 to account for friction [65]. Hard, normal contact with no separation between the surfaces after contact was further specified. No separation was chosen in an attempt to keep the cell periphery from lifting off of the substrate. As such, the observed behaviour where cells span concave surfaces ($K > 0,\ H > 0$) cannot be simulated in this work [36]. Tie constraints were used to constrain the nucleus to the CSK, and the CSK to the actin cortex. However, as previously mentioned, this constraint was avoided for the stress fibres, and the embedded constraint was utilised instead.

2-4 Simulation Steps

A static analysis was utilised to perform the simulation. The initial configuration comprises the undeformed spread cell placed above the substrate as shown in Figure 2-6. The complete simulation contained three steps, based on the work conducted by Vassaux et al. [43]. In step one, three external forces were applied to the cell: gravity, the force from the weight of the medium and the force from the AFM tip pressing the cell down. These loads pushed the hMSC onto the substrate, forcing the cell to conform to the surface curvature of the substrate. Step two removed the force from the AFM tip, allowing the hMSC to reach an equilibrium state. The FAs were also constrained in all degrees of freedom (DOF), representing the mechanical link between the FA and the substrate. Finally, in step three, a prestress was applied to the stress fibres of the cell, causing them to contract and apply forces to the FAs and nucleus.

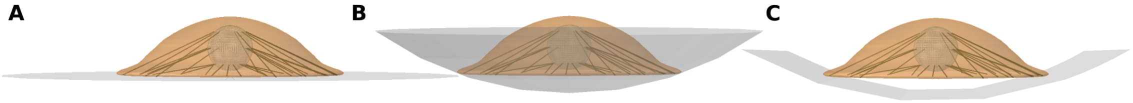

Figure 2-6: Undeformed hMSC on the three different types of substrates. **A:** Flat. **B:** Hemispherical ($\kappa = 1/75\ \mu m^{-1}$). **C:** Cylindrical ($\kappa = 1/75\ \mu m^{-1}$).

2-5 Boundary Conditions and Loads

In every simulation, the substrate was constrained in all degrees of freedom DOF, while the cell was left unconstrained. Once the cell conforms to the surface curvature of the substrate, the focal adhesions were constrained in all DOF. These constraints represent the mechanical link between the FA and the substrate.

Three external forces, a gravitational force, a pressure due to the weight of the culture medium and a force representing the pressure of the AFM tip, were applied to the cell. The two former forces remained active for all simulation steps, while the latter force was only applied in the first step. The gravitational force is defined using the gravitational load option in Abaqus and a vertical downwards acceleration of $-9.81\ m/s^2$. The load from the weight of the culture medium was included in the simulation as cells cultured in different media facilitating their growth, experience a force pressing the cell down by the parts of the medium directly above the cell [66, 67]. The total pressure was calculated as 1Pa using Equation 2-6.

$$pressure = \frac{mass * gravity}{area} \tag{2-6}$$

Where the mass was calculated as $mass = density * volume$. The density is the same as for water ($\rho = 1000\ kg/m^3$), and the volume was calculated based on an area of $1965\ \mu m^2$ and medium height of 10 μm [68]. The pressure ws applied to the superior area of the cell as shown in Figure 2-7A.

In line with previous research, [46], the force representing the AFM tip had a magnitude of roughly 50 nN and was applied to the cell using the surface traction option in Abaqus. The force was applied to a spherical area with a diameter of 8 μm at the central apex of the actin cortex, as shown in Figure 2-7A. This force pushed the cell down onto the substrate and ensured continuous contact. When the surface curvature increased to values $\kappa > 1/150\ \mu m^{-1}$, this force was not sufficient. Consequently, the force was increased to 150 nN, and the area over which it was applied was increased to a diameter of 16 μm. Two analyses were run for the cell on the flat substrate to allow both scenarios to be compared with the flat surface. In the first analysis, the AFM force equated to 50 nN; in the second, the same force had a magnitude of 150 nN. However, the analyses with the larger AFM tip force are expected to produce less reliable results.

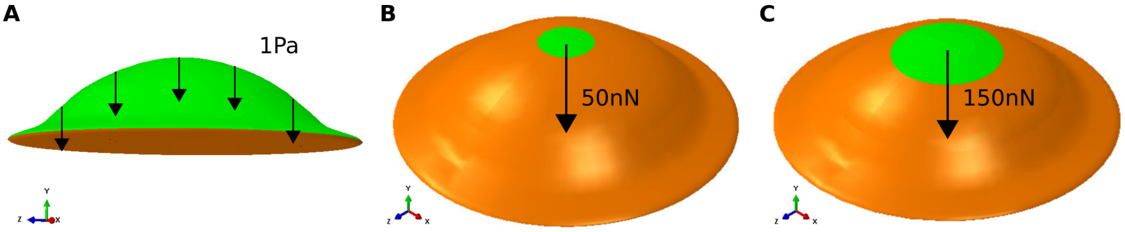

Figure 2-7: Schematic of cell, the green area represents the area where load was applied. **A:** A traction pressure of 1 Pa, representing the weight of the growth medium, was applied to the superior surface of the cell. **B & C:** the AFM force, representing the force from the AFM tip pushing the cell onto the substrate, was applied as a traction pressure of 50 nN (**B**) and 150 nN (**C**). The diameter of the green area is 8 µm (**B**) and 16 µm (**C**).

Finally, a prestress was applied to the stress fibres in the last step. In literature, it has been reported that stress fibres may experience prestress forces of up to 10 nN [69]. Using Equation 2-7, it was calculated that a temperature of -121 K corresponds to 10 nN contraction [70].

$$C = \frac{F}{c \times E \times A} \tag{2-7}$$

Where C represents the temperature, F constitutes the prestress applied to the SF, c is the coefficient of linear expansion of the SF, E is the modulus of elasticity of the SF, and A is the cross-sectional area of the SF.

2-6 Mesh

The nucleus and CSK were modelled using 11,040 and 188,332 linear hexahedral elements (C3D8H), respectively. The hybrid formulation was included to account for incompressibility. The actin cortex was represented by 57,086 triangular shell elements (S3), while 1,202 truss elements (T3D2) were used for the stress fibres. A mesh convergence and validation study were subsequently conducted (see appendix A-0-1). In total, 257,660 elements were used in the simulations with an average length of 0.4µm.

2-7 Readouts and Data Processing

Raw data relating to cellular traction forces, cell height, the stress of the actin cortex, and nuclear dimensions were extracted from the model and processed using Matlab 2020b (Figure 2-8). A full overview of the model workflow, highlighting model inputs and outputs, is given in Figure 2-8. A distinction was made between total traction forces and resultant traction forces. Total traction forces were defined as the sum of the absolute magnitude of all traction forces such that $|\vec{T_X}| + (|-\vec{T_X}|) = 2\vec{T_X}$. Where $\vec{T_X}$ is a traction force of magnitude T acting parallel to the x-axis. The resultant traction forces were defined as the sum of all traction forces so $\vec{T_X} + (-\vec{T_X}) = 0$. The total traction forces show the overall magnitude of forces acting on the cell, and can via the tensegrity theorem be related to the cell stiffness and stability [71]. The resultant traction forces provides an overview of the balance of the traction forces acting on the cell can be associated with cell migration [43]. Further, a statistical analysis in the form of ANOVA (Analysis of significant variance) was performed to investigate whether the surface curvature had an effect of statistical significance on the traction forces experienced by each FA [72]. The significance level was set to $p = 0.05$. Most results are presented with the outcomes for the hemispherical and cylindrical substrates normalised w.r.t the flat substrates.

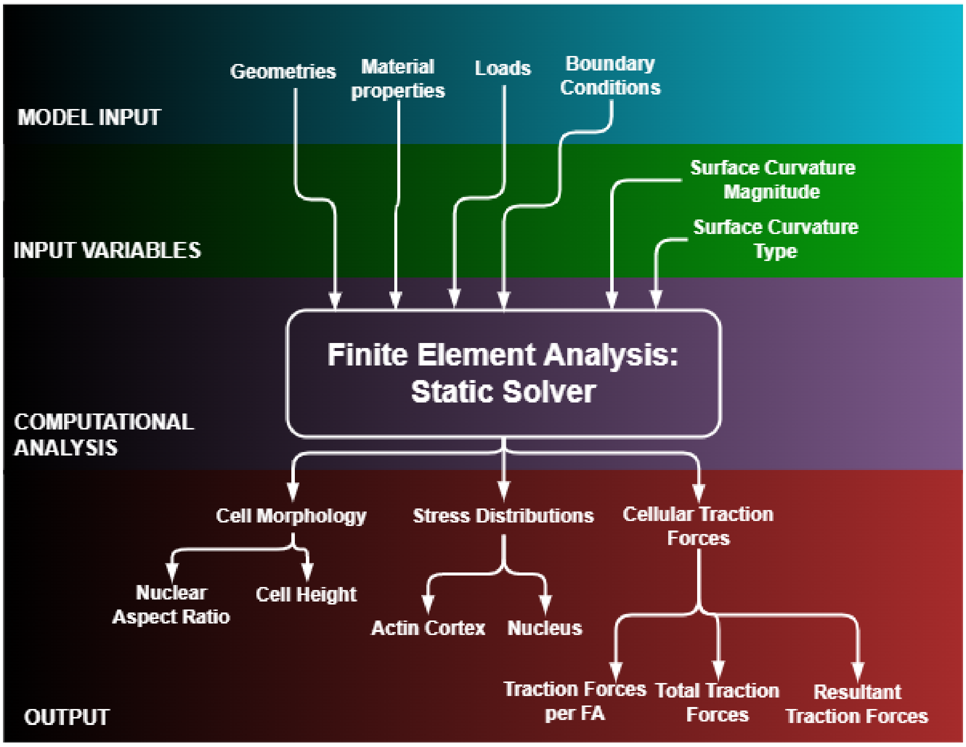

Figure 2-8: Schematic showing input parameters and input variables used in the FEA and specifies the different output types studied.

Chapter 3

Results

3-1 Traction Forces

3-1-1 FA Traction Forces are Similar for All Surfaces

The median traction forces remain similar for all surface types and surface curvatures as evident from Figure 3-1A and Figure 3-1B. The maximum traction forces have similar values with a maximum difference of 0.45nN between the cylindrical surface of $\kappa = 1/150\ \mu m^{-1}$ and the hemispherical surface of $\kappa = 1/150\ \mu m^{-1}$, and a maximum difference of 1.02 nN between the flat and hemispherical surface of $\kappa = 75\ \mu m^{-1}$. A more considerable variation is observed between the minimum traction forces, with a difference of 1.52 nN between the hemispherical surface of $\kappa = 1/250\ \mu m^{-1}$ and the hemispherical surface of $\kappa = 200\ \mu m^{-1}$, and a maximum difference of 2.14 nN between the flat and hemispherical surface of $\kappa = 1/75\ \mu m^{-1}$. Overall, the cell experience higher traction forces in the analyses where the force representing the AFM tip had a value of 150 nN. Neither the type nor the degree of curvature had an effect on the traction forces experienced by the FAs of statistical significance ($p < 0.05$).

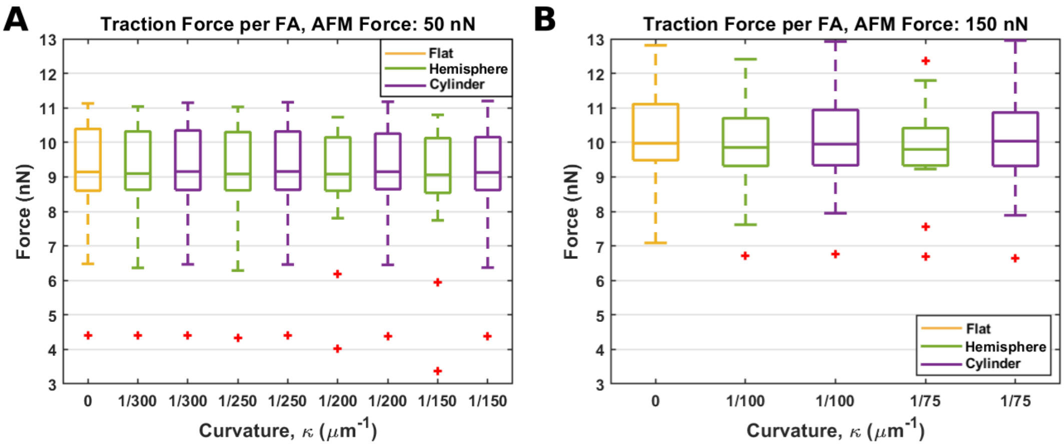

Figure 3-1: Boxplots of the traction forces experienced per focal adhesion for the different substrate types and degrees of curvature. The top and bottom edges of the boxes indicate the 25th and 75th percentage, while the central mark indicates the median. The red dots mark the outlier values. **A:** curvatures from $\kappa = 0\ \mu m^{-1}$ to $1/150\ \mu m^{-1}$. **B:** curvatures from $\kappa = 0\ \mu m^{-1}$ to $1/75\ \mu m^{-1}$

3-1-2 Total Cellular Traction Forces Decrease as Surface Curvature Increases

The total traction force the cell exerts on the substrate shows a slight reduction as the surface curvature increase (Figure 3-2). The total traction force reduces by approximately 2% as the surface curvature for the hemispherical substrate increase from $\kappa = 0\mu m^{-1}$ to $\kappa = 1/150\mu m^{-1}$ as shown in Figure 3-2A. The traction forces exerted on the cylindrical substrate decrease at

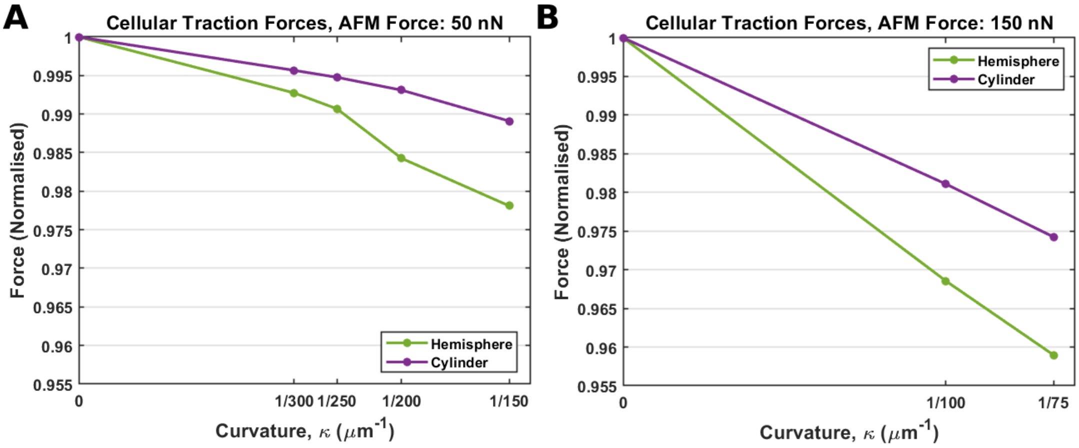

Figure 3-2: Cellular traction forces normalised w.r.t the flat surfaces plotted as a function of curvature. **A:** curvatures from $\kappa = 0\mu m^{-1}$ to $1/150\mu m^{-1}$. **B:** curvatures from $\kappa = 0\mu m^{-1}$ to $1/75\mu m^{-1}$.

half the rate and reduce by approximately 1% for the same increase in surface curvature. Similarly, the total traction forces decrease by approximately 4% and 2.5% for the hemispherical and cylindrical substrate, respectively, as the surface curvature increase from $\kappa = 0\mu m^{-1}$ to $\kappa = 1/75\mu m^{-1}$ as shown in Figure 3-2B. This reduction in traction forces indicates that the SFs become less tense as the curvature increases.

3-1-3 Central FAs Experience the Lowest Magnitude of Traction Forces

The mean magnitude of traction forces experienced by the FAs largely depends on the location of the focal adhesions as evident in Figure 3-3. For the substrates with curvatures $\kappa = 0\ \mu m^{-1}$ to $1/150\ \mu m^{-1}$ (Figure 3-3 A&B), the central FAs experience traction forces 85% the magnitude of the distal FAs. The medial FAs experience the most significant traction forces, 5% larger than the distal FAs. Independent of curvature, the cell appears to experience more significant traction forces towards the periphery of the cell. As the curvature increases, the average traction forces decrease slightly for all FA groups. The traction forces for the hemispherical substrate decrease at twice the rate compared to the cylindrical substrate. Similar observations are made for the cell resting on substrates with curvatures of $\kappa = 0\ \mu m^{-1}$ to $1/75\ \mu m^{-1}$ (Figure 3-3 C & D); the central FAs experience traction forces 92% the magnitude of the distal FAs. The medial FAs experience the most significant traction forces, 8% larger than the distal FAs. However, the traction forces experienced by the central FAs do not change significantly as the curvature increases from $\kappa = 1/100\ \mu m^{-1}$ to $1/75\ \mu m^{-1}$, indicating that there exists a threshold where they stop being sensitive to curvature.

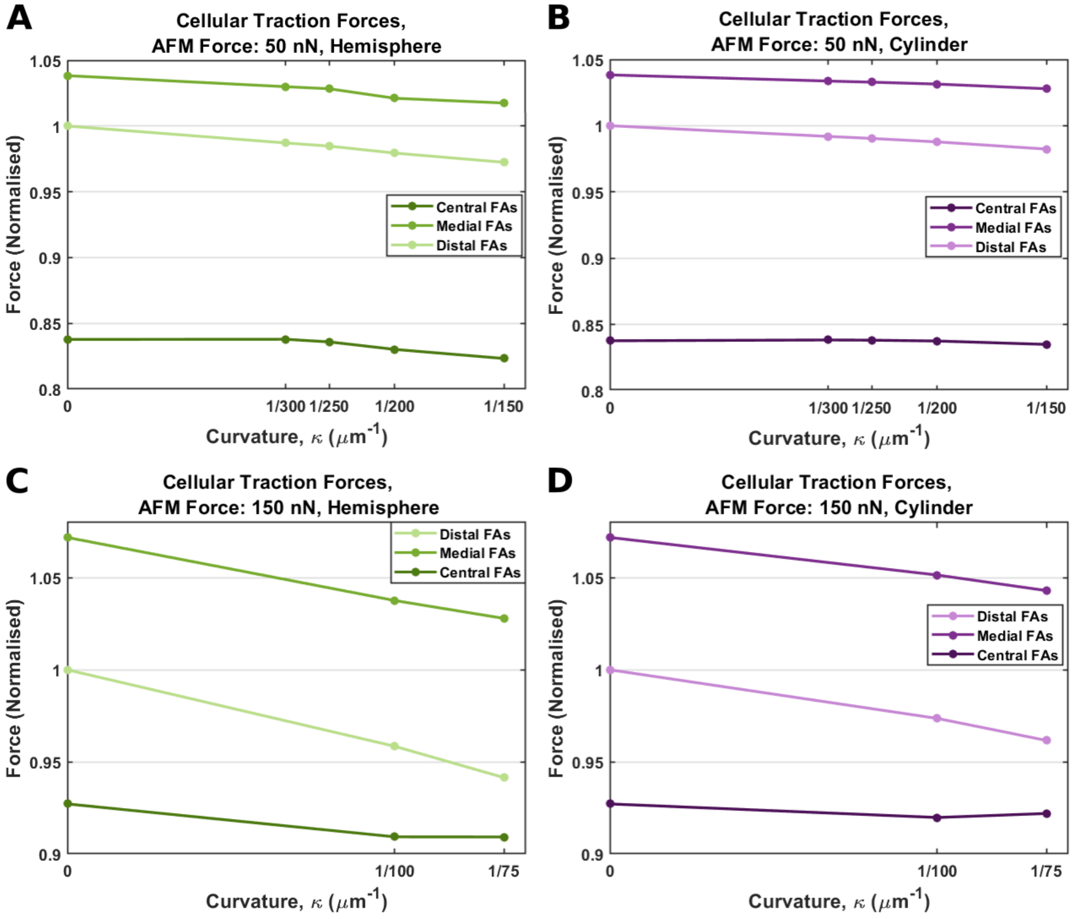

Figure 3-3: Plots showing traction forces normalised w.r.t the flat surfaces for the cell on hemispherical and cylindrical substrate of increasing curvature. **A&B:** curvatures from $\kappa = 0$ μm^{-1} to $1/150$ μm^{-1}. **C&D:** curvatures from $\kappa = 0$ μm^{-1} to $1/75$ μm^{-1}.

3-1-4 Resultant Vertical Traction Forces are Dependent on Surface Curvature

The resultant traction forces are non-zero for all substrates shown in Figure 3-4A and 3-4D, indicating that the traction forces exerted by the cell are not balanced. The resultant traction forces reduce significantly as the curvature increase. This decrease is most prominent for the hemispherical substrates, decreasing at almost twice the rate of the cylindrical substrates. Separating the resultant traction forces into their axial components, it is evident that the overall reduction is caused by the decrease in vertical traction forces (forces acting parallel to the Y-axis). The vertical traction forces exerted by the cell onto the substrate also push the cell onto the substrate, shown in Figure 3-5. These results indicate that as surface curvature increases, the cell encounters lower traction forces pushing it down onto the substrate. For both the

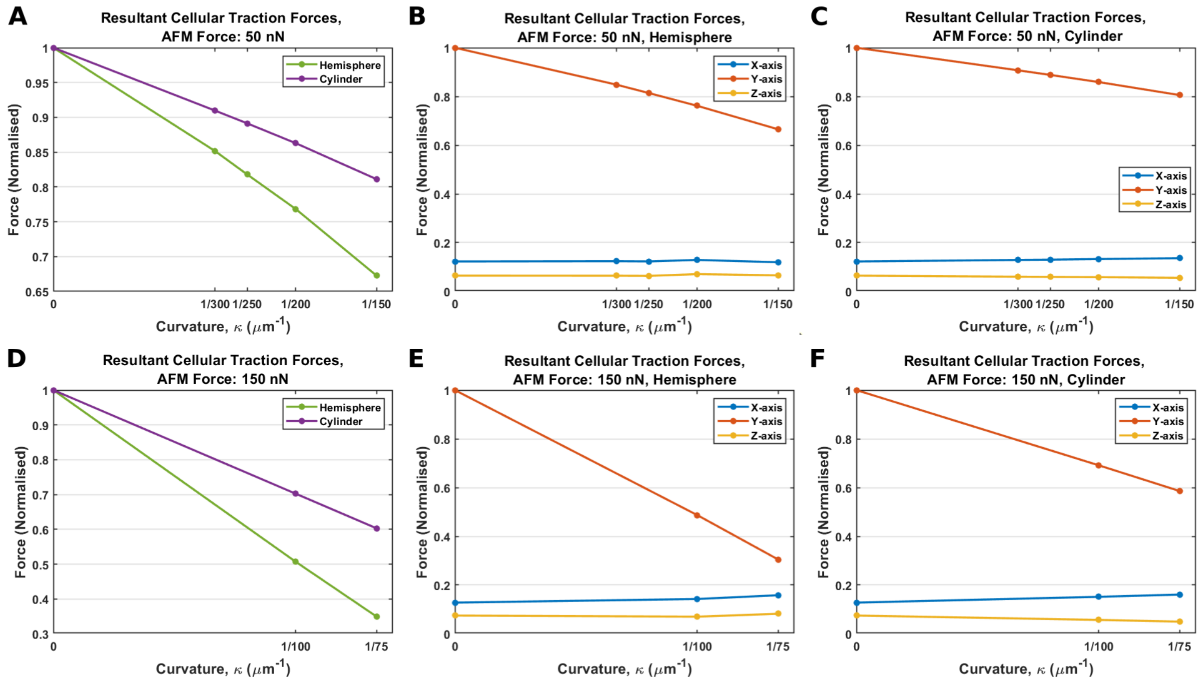

Figure 3-4: Plots resultant traction forces normalised w.r.t the flat surfaces plotted as a function of curvature. **A:** curvatures from $\kappa = 0\ \mu m^{-1}$ to $1/150\ \mu m^{-1}$. **B&C:** The resultant force split into its axial components for hemispherical and cylindrical substrates of curvatures from $\kappa = 0\ \mu m^{-1}$ to $1/150\ \mu m^{-1}$, respectively. **D:** curvatures from $\kappa = 0\ \mu m^{-1}$ to $1/75\ \mu m^{-1}$. **E&F:** The resultant force split into its axial components for hemispherical and cylindrical substrates of curvatures from $\kappa = 0\ \mu m^{-1}$ to $1/75\ \mu m^{-1}$, respectively.

hemispherical and cylindrical substrates, the horizontal traction forces (acting along the X-axis and Z-axis) appear unaffected by substrate curvature. Moreover the traction forces acting along the X-axis and Z-axis are not identical, with the magnitude of traction forces along the Z-axis being 42% to 69% less than the traction forces acting along the X-axis.

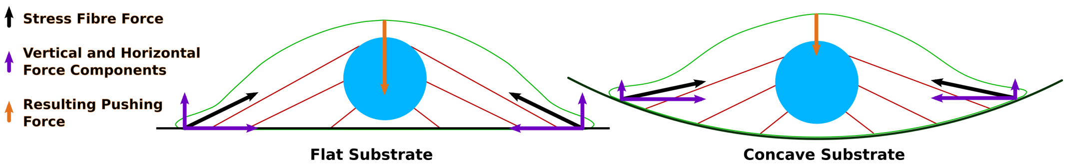

Figure 3-5: Schematic showing how resultant forces affect cells on flat and concave substrates. The green outline represents the overall morphology of the cell; the nuclei are shown in blue, while the actin stress fibres are depicted in red. The schematic is an ideal 2D representation where the horizontal forces are of equal magnitude and opposite direction and balance each other. The vertical force pushing the cell onto the substrate is lower for the concave surface than for the flat surface. The schematic is adapted from Werner et al. [36]

3-2 Stress of the Actin Cortex

The von Mises stress of the surface of the actin cortex in contact with the substrates appear dependent on curvature as shown in Figures 3-6 and 3-7. It is exceptionally high for the substrates with a surface curvature of $\kappa = 1/100\ \mu m^{-1}$ and $\kappa = 1/75\ \mu m^{-1}$. The most significant stress values are concentrated in the cortex's central area and diminish towards the periphery.

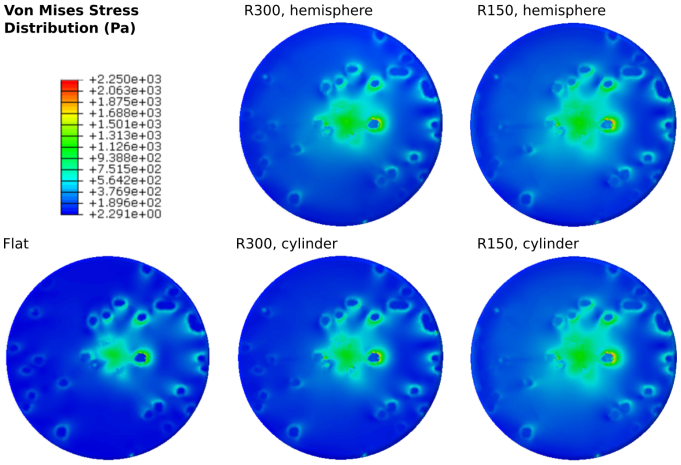

Figure 3-6: Von Mises stress distribution of the surface of the actin cortex in contact with the substrate. Cells on flat, hemispherical and cylindrical surfaces are shown, curvatures are limited to $\kappa = 1/300\ \mu m^{-1}$ and $\kappa = 1/150\ \mu m^{-1}$.

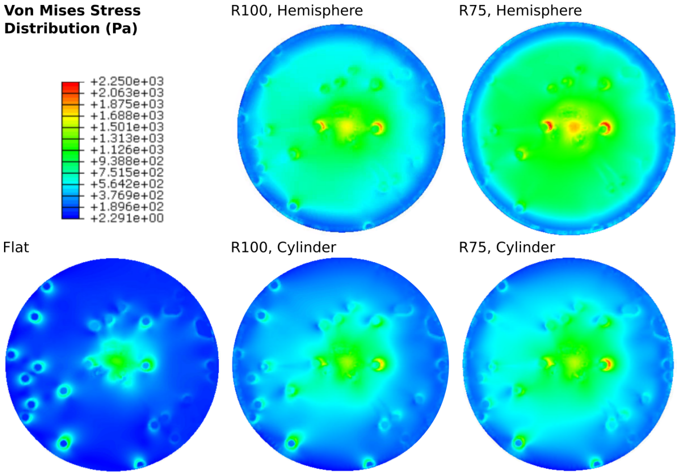

Figure 3-7: Von Mises stress distribution of the surface of the actin cortex in contact with the substrate. Cells on flat, hemispherical and cylindrical surfaces are shown, curvatures are limited to $\kappa = 1/100\ \mu m^{-1}$ and $\kappa = 1/75\ \mu m^{-1}$.

A lower von Mises stress is observed in the FA areas of the actin cortex, as these areas are constrained in all directions and unable to move relative to each other. However, Section 3-1 shows that the FA experience significant reaction forces. The normalised mean von Mises stress of the FAs are plotted in Figure 3-8. The stress experienced by the FAs increases considerably with curvature; the mean von Mises stress for the hemispherical substrate increases by almost 260% as the curvature increases from $\kappa = 0 \mu m^{-1}$ to $\kappa = 1/150 \mu m^{-1}$. The mean von Mises stress increases by nearly 190% for the cylindrical substrates for the same degree of curvature. Similarly, the average von Mises stress increase by 290% as the curvature increase from $\kappa = 0 \mu m^{-1}$ to $\kappa = 1/75 \mu m^{-1}$, while it increases by nearly 220% for the cylindrical substrates for the same degree of curvature.

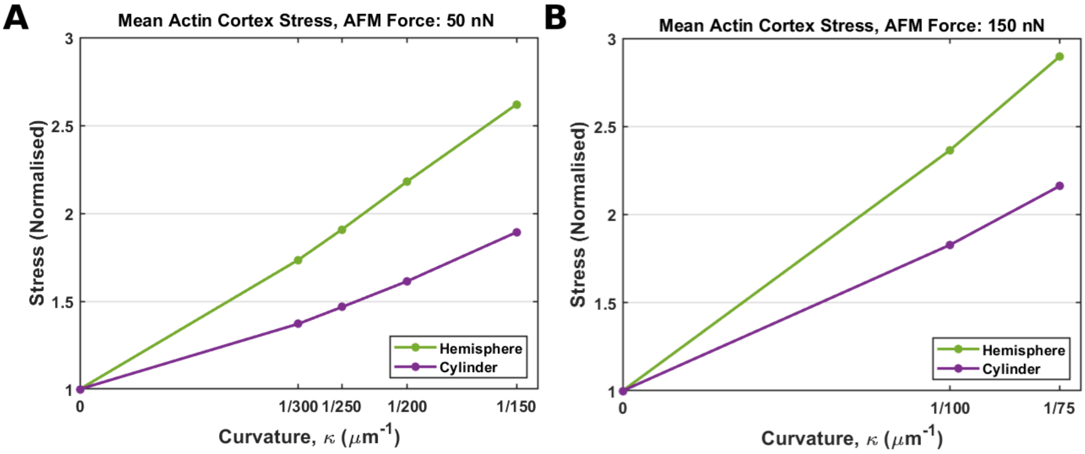

Figure 3-8: Average Von Mises stress for the FA areas of the actin cortex normalised w.r.t the flat surfaces plotted as a function of curvature. **A:** curvatures from $\kappa = 0\ \mu m^{-1}$ to $1/150$ μm^{-1}. **B:** curvatures from $\kappa = 0\ \mu m^{-1}$ to $1/75\ \mu m^{-1}$.

3-3 Cell Morphology

The overall morphology of the hMSC was not heavily influenced by the contracted SFs (See appendix B). The overall morphologies of the cell conformed onto the flat, cylindrical, and hemispherical substrates after the prestress were applied to the SF are shown in Figure 3-9.

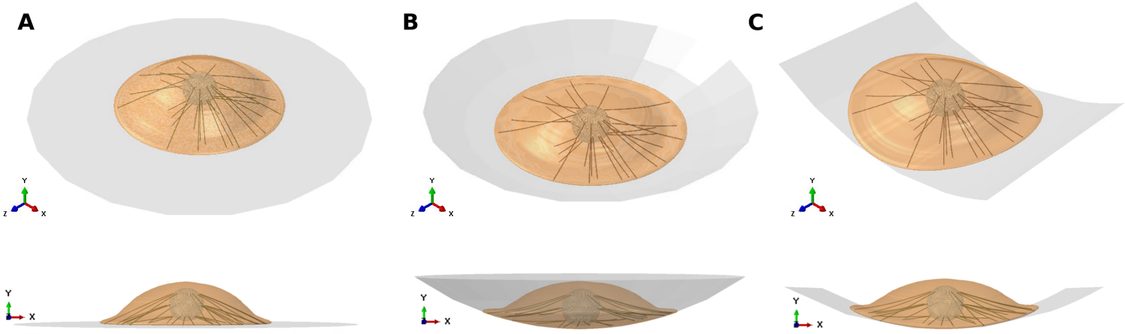

Figure 3-9: Orthogonal and lateral views of the hMSC spread on the three different types of substrates. **A:** Flat. **B:** Hemispherical ($\kappa = 1/75\ \mu m^{-1}$). **C:** Cylindrical ($\kappa = 1/75\ \mu m^{-1}$).

The maximum height of the cell was observed to increase with curvature as shown in Figure 3-10A and 3-10B. Moreover, the hemispherical substrates appear to have a greater influence on cell height compared to the cylindrical substrates. However, the overall effect of curvature seems negligible as the biggest increase in height is approximately 0.3 µm as the hemispherical substrate increase in curvature from $\kappa = 0\ \mu m^{-1}$ to $\kappa = 1/75\ \mu m^{-1}$.

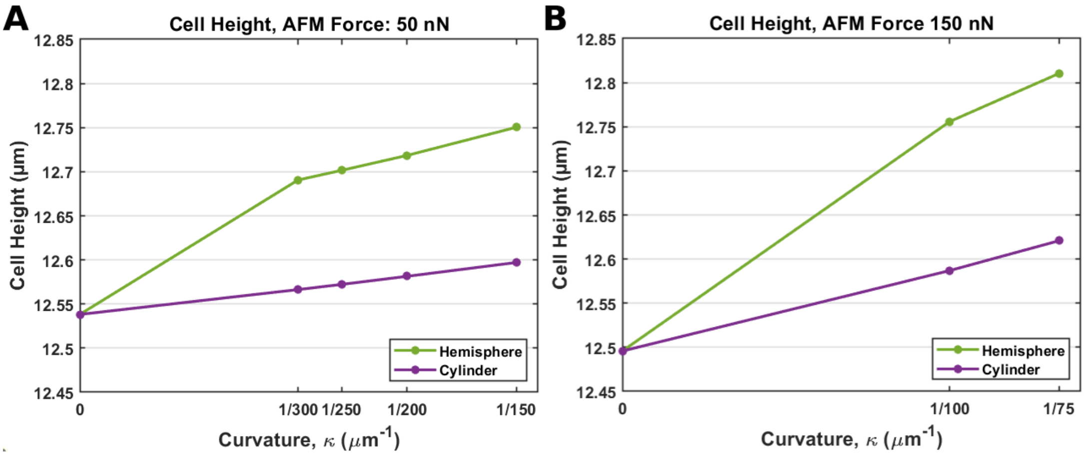

Figure 3-10: Cell height plotted as a function of curvature. **A:** curvatures from $\kappa = 0\ \mu m^{-1}$ to $1/150\ \mu m^{-1}$. **B:** curvatures from $\kappa = 0\ \mu m^{-1}$ to $1/75\ \mu m^{-1}$.

3-4 Stress and Deformation of Nucleus

The areas where the SFs tether the nucleus experience large stresses and deformations as shown in Figure 3-11. The model description utilised the embedded constraint to avoid tying stress fibres to specific nuclear nodes and causing large, unrealistic stresses. However, unrealistic stresses are present in the form of sharp, cone-shaped pillars protruding from the nucleus, as shown in Figure 3-11. Excluding the cone-shaped pillars, it is also evident from Figure 3-11 that the stress concentrations appear in small areas where the actin SFs tether the nuclei. However, there does not seem to be a noticeable difference in stress distribution or magnitude as the curvature increases. The nuclear aspect ratio is calculated to investigate how curvature affects the nucleus. The aspect ratio is determined as the nuclear height to width ratio. When the ratio decreases, the nucleus flattens, and the nucleus becomes elongated when the ratio increases. A ratio of one means that the nucleus has a spherical shape. In the present work, the width is determined as an average of multiple widths across the transverse midplane of the nucleus. The nodes experiencing the most extreme stresses were not considered in an attempt to get a more realistic image of the aspect ratio. The results are plotted in Figures 3-12A and 3-12B. The nuclear aspect ratio appears proportional to curvature, and the nucleus becomes more spherical for substrates of higher curvature. The aspect ratio is more sensitive to the hemispherical substrate than the cylindrical substrate. However, similar to the cell height, the

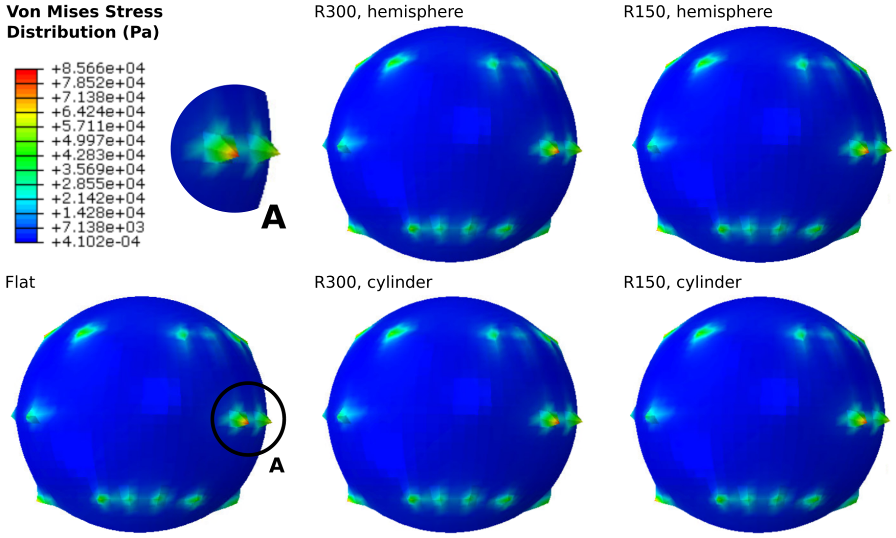

Figure 3-11: Stress distribution for nucleus on hemispherical and cylindrical substrates of curvatures $\kappa = 0\ \mu m^{-1}$, $\kappa = 1/300\ \mu m^{-1}$ and $\kappa = 1/150\ \mu m^{-1}$. There is no noticeable difference of the stress distributions between the different nuclei. Detail A highlights an area where unrealistic stresses and deformation occur.

increase in the aspect ratio is minuscule. The maximum rise is approximately 1.5% as the curvature increase from $\kappa = 0\ \mu m^{-1}$ to $\kappa = 75\ \mu m^{-1}$. The present curvatures have a limited influence on nuclear morphology.

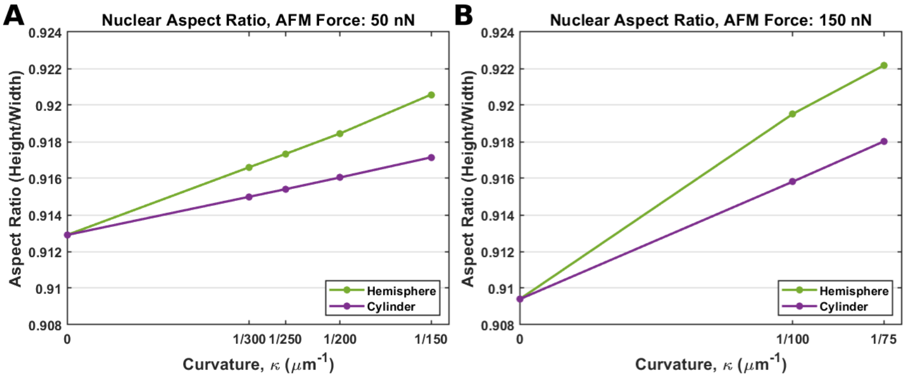

Figure 3-12: The nuclear aspect ratio plotted as a function of curvature. **A:** curvatures from $\kappa = 0\ \mu m^{-1}$ to $1/150\ \mu m^{-1}$. **B:** curvatures from $\kappa = 0\ \mu m^{-1}$ to $1/75\ \mu m^{-1}$.

Chapter 4

Discussion

The present study's primary objectives were to investigate if different substrate curvatures induced different reactions to cellular traction forces and cellular morphology. In the quantified results, the influence of curvature often had little effect on many of the output variables investigated. The cell height increased with a maximum of 0.3 µm, while the overall traction forces varied with a maximum of 4%. These observation is in line with results reported in literature [43, 73]. Xi observed *in vitro* that the average cell height of epithelial cells increased by approximately 0.2 µm as the curvature of concave cylindrical substrates increased from 0 to $1/150\ \mu m^{-1}$ [73]. However, the cell height increased by more than 2 µm as the degree of curvature increased to $1/25\ \mu m^{-1}$. *In silico*, Vassaux and Milan reported that within the $\kappa = 0$ to $\kappa = 1/150\ \mu m^{-1}$ range of concave hemispherical substrates, the difference in total stress fibre forces was closer to 5%, while the differences in nuclear strain were considered negligible [43].

The cellular response was more pronounced for the cell on the hemispherical substrates than the cell on the cylindrical substrates. Hemispherical substrates have a constant curvature along all axes, while cylindrical substrates exhibit a direction of zero curvature perpendicular to the direction of maximum curvature. As such, the cylindrical substrates possess similar qualities to the hemispherical substrates along the direction of maximum curvature and similar qualities to the flat substrate along the direction of zero curvature. Therefore, the observation that the cell on the cylindrical substrate yields less elevated responses than on the hemispherical substrates is in line with expectations.

An increase in curvature appears to be inversely correlated with cellular traction forces. Lower traction forces reflect a less tense cytoskeleton. According to the tensegrity theorem, a reduction in tension of the cytoskeleton results in an overall less stiff cell [71]. A reduction in overall stiffness reduces the cell's stability, a factor known to induce apoptosis and inhibit differentiation [74]. As such, it is tempting to deduce that hMSCs will try to avoid areas of concave surface curvature. However, the overall reduction in traction forces was minuscule, and though the curvature had an effect, it was minor and not statistically significant. Moreover, in vitro hMSCs are observed to actively migrate towards concave pits [36, 75]. Mechanically, concave topographies act as stable equilibrium configurations, minimising potential energy [43].

The resultant traction forces decrease considerably as the degree of curvature increases. This is in line with previous *in silico* observations [43] and is largely due to the decrease in vertical traction forces. When the curvature increases, the forces pushing the cell down onto the substrate diminishes. As the curvature continue to increase, a threshold will eventually be reached where the vertical traction forces begin to pull the cell upwards, providing a lifting force. Werner et al. noted that for all concave hemispherical curvatures ($\kappa = 1/375\ \mu m^{-1}$, $1/250\ \mu m^{-1}$, $1/175\ \mu m^{-1}$, $1/125\ \mu m^{-1}$), hMSCs spanned the surface, minimising its contact points with the surface [36]. According to the chord model developed by Bidan et al., cells are defined as tensile elements that will stretch upwards when attached to concave substrates [76]. Results from the present study agree with this theory, and the reduction in vertical traction force pushing the cell down onto the substrate is likely a significant contributing factor to this phenomenon. The resultant horizontal traction forces' sensitivity to curvature is far more limited than the resultant vertical traction forces, remaining virtually constant. The overall presence of horizontal traction forces indicates that the cell pulls itself slightly in a specific direction. This is behaviour that is typically observed in migratory cells [77]. The non-uniform distribution of the actin SFs throughout the cell is the cause of the non-zero resultant horizontal forces. Indeed, in the work of Vassaux, where traction forces are averaged over many cells, approximating a uniform actin SF distribution, the resultant horizontal traction forces are zero [43]. However, on an individual cell level, non-uniform distributions of SF and focal adhesions are observed in vitro [77]. In particular, a large density of smaller focal adhesions are observed close to the cell's leading edge, an area that generates larger traction forces and is the main driving force in cell migration [78]. The areas with a higher FA density, and a consequent surplus of horizontal traction forces, could signify the initiation of a leading edge. This is in line with the present work, where it is shown that the medial and distal focal adhesions experience larger traction forces compared to the central FAs. Moreover, the non-uniform distribution of FAs and SFs, with the majority aligned along the X-axis, results in larger horizontal traction forces acting along the same axis.

In literature, it has been reported that the location of the FA is a crucial deciding factor in the amount of traction force the FA experiences [77]. Typically, the most significant traction forces are generated in the FAs close to the cell periphery and leading-edge. In contrast, the lowest magnitudes are generated in FAs towards the centre of the cell. In the present study, it is accordingly observed that the central FAs experience the lowest traction forces. However, contrastingly, the medial FAs appear to generate traction forces 5% larger in magnitude than the distal FAs. This behaviour is observed independent of curvature. An explanation could lie within the model design; firstly, the average distances to the centre of the cell are $23.6 \pm 0.53\ \mu m$, $20.7 \pm 1.46\ \mu m$ and $12 \pm 4.06\ \mu m$ for the distal, medial, and central FA groups, respectively. The distal and medial FAs are located at a reasonably similar distance to the centre of the cell and would be expected to experience quite similar traction forces. Secondly, due to the non-uniform stress fibre distribution, the nucleus is pulled in one direction. This results in extra tensile forces exerted on the stress fibres that the nucleus is moving away from. The majority of the FAs experiencing these extra tensional forces are medial FAs, resulting in this group experiencing larger tensile forces than the distal group.The traction forces experienced by each FA group are somewhat dependent on curvature, with each group expressing a greater sensitivity to the hemispherical substrate than the cylindrical substrate. The central FAs seem the least sensitive to curvature, with traction forces only noticeably reducing for hemispherical substrates of a higher degree of curvature ($\kappa < 1/250\ \mu m^{-1}$). The sensitivity to higher degrees of curvature and the low magnitude of traction forces experienced by central FAs may explain in vitro observations showing that hMSCs on concave surfaces express a low density of FA in the perinuclear area [36]. It is known that an increase or decrease in traction forces may cause the FA to enlarge or disassemble, respectively [13]. Therefore, the central FAs may disappear in response to the low magnitude of traction forces experienced. The observation that central FAs experience lower traction forces further substantiates the phenomenon where hMSCs span concave surfaces.

A significant observation in the present study is the correlation between stress experienced by the actin cortex and the curvature. Specifically, the magnitude and distribution of stress of the actin cortex in contact with the surface appear proportional to an increase in curvature. This stress increase may be an underlying cause of why hMSCs prefer to span concave; hemispherical substrates [36]. The cell can reduce its surface area and avoid larger deformations by lifting off the substrate.

The cell height is observed to be proportional to the degree of curvature. A higher degree of curvature yields a minor increase in height. The effect is most prevalent on the hemispherical substrate, with the cell on the cylindrical substrate seemingly less sensitive to curvature. This is in line with observations made by Xi et al., where epithelial cells seeded on the concave face of cylinders expressed a similar lack of sensitivity to curvatures of similar degrees [73]. The Prockop group [79–83] have reported that MSCs can be separated into two morphological types; rapidly proliferating, small, round cells (RS cells), and slowly proliferating, large flattened cells (FC) [82]. In general, the RS cells that manifest a higher degree of multipotency exhibit a larger cell height than the FC cells [84]. Observations from the present work are not significant enough to suggest that substrate curvature alters the cellular morphology sufficiently to change the cell phenotype. However, it is likely that hemispherical substrates of higher degrees of curvature will limit the cell's opportunity to spread. It should therefore be investigated whether meso-scale curvature can produce cell cultures where most cells retain their multipotency. On the contrary, it has also been reported that taller adipose-derived MSCs express a preference for adipogenic differentiation [85, 86], while flatter, spread hMSC on convex substrates have shown a preference for osteogenic differentiation [36]. Consequently, more research is necessary to determine how surface curvature affects cell differentiation.

The present work observed that surface curvature had a minor effect on the nuclear aspect ratio. As the degree of curvature decreases, the nucleus flattens. This observation is similar, but less pronounced, to what has been reported in the literature [35]. It has been shown that changes in nuclear strain can lead to chromatin deformation and alter gene transcription [87]. Nuclei located on concave substrates have been found to contain more condensed chromatin and cytoplasmic YAP (a central regulator of cell proliferation [88]) compared to nuclei on flatter, and convex substrates [89]. However, the nuclear envelope is wrinkled and folded and can easily provide more surface area without a comparable increase in stress [90]. As such, whether the nuclear strains observed in the present work are sufficient to alter chromatin conformation and, subsequently, gene transcription and cell fate remain elusive.

The degree and type of curvature appeared to have little effect on the stresses experienced by the nucleus. In literature, it has been reported that the nuclear stress is inversely correlated with the degree of curvature for concave hemispherical surfaces [43]. As such, the nucleus appears more stable on concave surfaces than on flatter surfaces. This may play a part in why hMSCs chose to migrate into concave pits [36]. The cell may prefer a more stable nucleus over the stability it derives from an overall increase in stiffness when resting on flat and convex surfaces. Pieuchot et al. suggest that migrating cells in curved environments follow the path of least nuclear mechanical stress [75]. The findings in the present work were not sufficient to support this theory.

4-1 Shortcomings and improvements of model

4-1-1 Reduce Extreme Nuclear Strains

The greatest observed weakness of the present model was the large, localised nuclear strains observed in the areas where the stress fibres link to the nucleus. The reason these strains occur appears to be twofold. Firstly, the nuclear mesh is coarse compared to the SF diameter (0.4 µm element length vs 0.25 µm SF diameter). The similarity in size results in the SFs transmitting all their force to one nuclear node. A simulation with a finer nuclear mesh (average element length 0.2 µm) was executed to investigate the effect of mesh refinement. The strains were observed to still be present, however, in a more rounded and less extreme manner. A more extensive mesh refinement should therefore reduce the strains considerably. Secondly, the cross-sectional area remains constant along the length of the SF, so it links to the nucleus over a minimal area and consequently distributes the contractile forces over this smaller area. This becomes more evident for the medial and central stress fibres that are angled in a more normal direction towards the nuclear surface. *In vivo* and *in vitro* SFs are linked to the nucleus and substrate through LINC complexes and FAs, respectively [91, 92]. These features have a larger cross-sectional area and distribute the contractile forces over larger areas. It would be preferred to model the SFs with tapered ends. This would result in a larger cross-sectional area linking the SF and the nucleus, which would improve the distribution of the contractile SF forces.

4-1-2 Improvements for Stress Fibres and CSK

As an objective of the present study was to investigate how surface curvature affects the nucleus, only stress fibres that are mechanically linked to the nucleus were modelled, mainly ventral and apical SF. Including the more peripheral transverse and dorsal SF would be more realistic. The apical and ventral SFs are also observed mechanically linked to the nucleus in many locations across a singular SF [15, 91]. Modelling each SF to only link to the nucleus in one location, the SF end, is a significant simplification. As the SFs are stochastically generated, the results from one cell do not necessarily represent actual cellular behaviour or the general case. This became evident regarding the medial FAs experiencing larger traction forces than the distal FAs. This effect would be reduced by generating multiple cells with stochastically distributed stress fibres. The averaged results for a large number of cells should yield results that approach zero resultant horizontal traction forces as observed by Vassaux [43]. SFs resist tensional forces; however, other cytoskeletal elements like microtubules and intermediate filaments equip the cell with resistance to compressive forces. It has also been observed that especially microtubules have the ability to influence nuclear morphology [15]. As a significant focus in this study was particularly on how surface curvature affects nuclear morphology, microtubules could favourably have been included in the model.

4-1-3 Focal Adhesions can be Represented by Cohesive Zone Models

The focal adhesions are modelled by constraining smaller areas of the actin cortex in all degrees of freedom once contact with the substrate is established. In vivo and in vitro, this is certainly not the case, and bonds between the integrins and substrate break if the forces get large enough [93]. An excellent way of modelling such behaviour is by implementing cohesive zone models (CZM) [94]. These phenomenological models have been developed to describe crack propagation between two surfaces. Such models describe the evolution of shear and normal traction forces and have been used in single-cell simulations in the past [54, 95]. However, as they can increase computational time drastically, they were not implemented in the present work.

4-1-4 Geometry and Material Models

The present model represents the general hMSC morphology and mechanical properties. Consequently, the geometrical properties in the cell model are simplified and idealised. Previously, cell geometry was recreated in great detail using scanned data from individual cells [96, 97] to produce more accurate results. However, this comes at the cost of computational time, and the results tend to represent only the scanned cell. Some accuracy is sacrificed by simplifying the cell geometry to save computational power.

The material descriptions used for this model were either hyperelastic or linear elastic. While hyperelasticity captures some of the mechanical qualities of cellular behaviour, it fails to include the time-dependent properties that have been observed [98, 99]. Viscoelastic material models, therefore, represent cells far better. Even stress fibres have been observed to exhibit viscoelastic behaviour [100]. For further development of the present model, it is consequently recommended to use viscoelastic material models.

Computational simulations often balance model complexity, model convergence, and computational cost. Complex models may produce results that align closer to the in vivo or in vitro state it aims to recreate. However, such models are often exceptionally computationally costly and often fail to converge. Consequently, while some of the shortcomings of the present model can be avoided by adding complexity, it is far from given that all additions will be beneficial.

Chapter 5

Conclusions and Recommendations

To the best of the author's knowledge, this is the only study that has utilised the finite element method to investigate how a cell with prestressed actin stress fibres interacts with substrates of meso-scale surface curvature. An hMSC was simulated on substrates with hemispherical and cylindrical concave surfaces with curvatures ranging from $\kappa = 0\ \mu m^{-1}$ to $\kappa = 1/75\ \mu m^{-1}$. The markers used to quantify cellular response comprised cellular traction forces, the nuclear aspect ratio and stress distributions, the cell height, and the stress distributions of the actin cortex. It was observed that the central FAs experienced lower traction forces than the other groups, indicating that the strength of the adhesive bonds between the cell and the substrate is lower in central areas. Moreover, the study revealed that the vertical traction forces pulling the cell onto the substrate reduce considerably as the curvature increases. The cell on the hemispherical substrates experienced a reduction in vertical traction forces at twice the rate compared to the cell on the cylindrical substrates. Finally, the stresses of the actin cortex increase considerably with the degree of curvature. The stresses experienced by the cell were more significant for the hemispherical substrates than the cylindrical substrates. Spanning the substrate and reducing the surface area in contact with the hemispherical substrates would help the cell avoid these stresses. Overall, these results support in vitro observations of hMSCs spanning concave hemispherical substrates. The present model shows that FEM can successfully be employed to predict certain aspects of hMSC behaviour on substrates with meso-scale surface curvature. However, the model did not find the variation of FA traction forces with curvature statistically significant. The primary cause is likely the narrow range of substrate surface curvatures investigated. More pronounced results are likely to be obtained for higher degrees of curvature. There is a lack of knowledge of cellular behaviour and fate on substrates with hyperbolic surfaces. Extending the present model to include such curvatures may provide valuable information.

Bibliography

[1] K. Ghosh and D. Ingber, “Micromechanical control of cell and tissue development: Implications for tissue engineering,” *Advanced Drug Delivery Reviews*, vol. 59, pp. 1306–1318, Nov. 2007.

[2] R. C. Dutta and A. K. Dutta, “Cell-interactive 3D-scaffold; advances and applications,” *Biotechnology Advances*, vol. 27, pp. 334–339, July 2009.

[3] J. Zhang, E. Wehrle, P. Adamek, G. R. Paul, X.-H. Qin, M. Rubert, and R. Müller, “Optimization of mechanical stiffness and cell density of 3D bioprinted cell-laden scaffolds improves extracellular matrix mineralization and cellular organization for bone tissue engineering,” *Acta Biomaterialia*, vol. 114, pp. 307–322, Sept. 2020.

[4] M. F. Pittenger, D. E. Discher, B. M. Péault, D. G. Phinney, J. M. Hare, and A. I. Caplan, “Mesenchymal stem cell perspective: cell biology to clinical progress,” *npj Regenerative Medicine*, vol. 4, p. 22, Dec. 2019.

[5] M. F. Pittenger, A. M. Mackay, S. C. Beck, R. K. Jaiswal, R. Douglas, J. D. Mosca, M. A. Moorman, D. W. Simonetti, S. Craig, and D. R. Marshak, “Multilineage Potential of Adult Human Mesenchymal Stem Cells,” *Science*, vol. 284, pp. 143–147, Apr. 1999.

[6] H. Gerardo, A. Lima, J. Carvalho, J. R. D. Ramos, S. Couceiro, R. D. M. Travasso, R. Pires das Neves, and M. Grãos, “Soft culture substrates favor stem-like cellular phenotype and facilitate reprogramming of human mesenchymal stem/stromal cells (hMSCs) through mechanotransduction,” *Scientific Reports*, vol. 9, p. 9086, Dec. 2019.

[7] R. J. Pelham and Y. L. Wang, “Cell Locomotion and Focal Adhesions Are Regulated by

the Mechanical Properties of the Substrate," *The Biological Bulletin*, vol. 194, pp. 348–350, June 1998.

[8] K. Anselme, "Osteoblast adhesion on biomaterials," *Biomaterials*, vol. 21, pp. 667–681, Apr. 2000.

[9] P. T. Caswell and T. Zech, "Actin-Based Cell Protrusion in a 3D Matrix," *Trends in Cell Biology*, vol. 28, pp. 823–834, Oct. 2018.

[10] S. Sugita, T. Adachi, Y. Ueki, and M. Sato, "A Novel Method for Measuring Tension Generated in Stress Fibers by Applying External Forces," *Biophysical Journal*, vol. 101, pp. 53–60, July 2011.

[11] A. D. Rape, W.-h. Guo, and Y.-l. Wang, "The regulation of traction force in relation to cell shape and focal adhesions," *Biomaterials*, vol. 32, pp. 2043–2051, Mar. 2011.

[12] K. Legerstee and A. Houtsmuller, "A Layered View on Focal Adhesions," *Biology*, vol. 10, p. 1189, Nov. 2021.

[13] K. Anselme, L. Ploux, and A. Ponche, "Cell/Material Interfaces: Influence of Surface Chemistry and Surface Topography on Cell Adhesion," *Journal of Adhesion Science and Technology*, vol. 24, pp. 831–852, Jan. 2010.

[14] A. dos Santos and C. P. Toseland, "Regulation of Nuclear Mechanics and the Impact on DNA Damage," *International Journal of Molecular Sciences*, vol. 22, p. 3178, Mar. 2021.

[15] Y. Kalukula, A. D. Stephens, J. Lammerding, and S. Gabriele, "Mechanics and functional consequences of nuclear deformations," *Nature Reviews Molecular Cell Biology*, May 2022.

[16] T. Andersen, D. Wörthmüller, D. Probst, I. Wang, P. Moreau, V. Fitzpatrick, T. Boudou, U. Schwarz, and M. Balland, "Cell size and actin architecture determine force generation in optogenetically activated adherent cells," preprint, Biophysics, Mar. 2022.

[17] A. Abbasi, S. Imaichi, V. Ling, and A. Shukla, "Mesenchymal Stem Cell Behavior on Soft Hydrogels with Aligned Surface Topographies," *ACS Applied Bio Materials*, vol. 5, pp. 1890–1900, May 2022.

[18] T. H. Qazi, D. J. Mooney, G. N. Duda, and S. Geissler, "Biomaterials that promote cell-cell interactions enhance the paracrine function of MSCs," *Biomaterials*, vol. 140, pp. 103–114, Sept. 2017.

[19] J. P. Winer, P. A. Janmey, M. E. McCormick, and M. Funaki, "Bone Marrow-Derived Human Mesenchymal Stem Cells Become Quiescent on Soft Substrates but Remain Responsive to Chemical or Mechanical Stimuli," *Tissue Engineering Part A*, vol. 15, pp. 147–154, Jan. 2009.

[20] G. S. Jeong, J. Y. Chang, J. S. Park, S.-A. Lee, D. Park, J. Woo, H. An, C. J. Lee, and S.-H. Lee, "Networked neural spheroid by neuro-bundle mimicking nervous system created by topology effect," *Molecular Brain*, vol. 8, p. 17, Dec. 2015.

[21] A. J. Engler, S. Sen, H. L. Sweeney, and D. E. Discher, "Matrix Elasticity Directs Stem Cell Lineage Specification," *Cell*, vol. 126, pp. 677–689, Aug. 2006.

[22] K. A. Kilian, B. Bugarija, B. T. Lahn, and M. Mrksich, "Geometric cues for directing the differentiation of mesenchymal stem cells," *Proceedings of the National Academy of Sciences*, vol. 107, pp. 4872–4877, Mar. 2010.

[23] J. Y. Park, D. H. Lee, E. J. Lee, and S.-H. Lee, "Study of cellular behaviors on concave and convex microstructures fabricated from elastic PDMS membranes," *Lab on a Chip*, vol. 9, no. 14, p. 2043, 2009.

[24] M. Rumpler, A. Woesz, J. W. Dunlop, J. T. van Dongen, and P. Fratzl, "The effect of geometry on three-dimensional tissue growth," *Journal of The Royal Society Interface*, vol. 5, pp. 1173–1180, Oct. 2008.

[25] S. Oh, K. S. Brammer, Y. S. J. Li, D. Teng, A. J. Engler, S. Chien, and S. Jin, "Stem cell fate dictated solely by altered nanotube dimension," *Proceedings of the National Academy of Sciences*, vol. 106, pp. 2130–2135, Feb. 2009.

[26] S. A. Ruiz and C. S. Chen, "Emergence of Patterned Stem Cell Differentiation Within Multicellular Structures," *Stem Cells*, vol. 26, pp. 2921–2927, Nov. 2008.

[27] Y.-P. Lo, Y.-S. Liu, M. G. Rimando, J. H.-C. Ho, K.-h. Lin, and O. K. Lee, "Three-dimensional spherical spatial boundary conditions differentially regulate osteogenic differentiation of mesenchymal stromal cells," *Scientific Reports*, vol. 6, p. 21253, Aug. 2016.

[28] Q. Li, A. Kumar, E. Makhija, and G. Shivashankar, "The regulation of dynamic mechanical coupling between actin cytoskeleton and nucleus by matrix geometry," *Biomaterials*, vol. 35, pp. 961–969, Jan. 2014.

[29] N. Jain, K. V. Iyer, A. Kumar, and G. V. Shivashankar, "Cell geometric constraints induce modular gene-expression patterns via redistribution of HDAC3 regulated by actomyosin

contractility," *Proceedings of the National Academy of Sciences*, vol. 110, pp. 11349–11354, July 2013.

[30] V. Malheiro, F. Lehner, V. Dinca, P. Hoffmann, and K. Maniura-Weber, "Convex and concave micro-structured silicone controls the shape, but not the polarization state of human macrophages," *Biomaterials Science*, vol. 4, no. 11, pp. 1562–1573, 2016.

[31] M.-H. Kim, Y. Sawada, M. Taya, and M. Kino-oka, "Influence of surface topography on the human epithelial cell response to micropatterned substrates with convex and concave architectures," *Journal of Biological Engineering*, vol. 8, p. 13, Dec. 2014.

[32] M. Théry, A. Pépin, E. Dressaire, Y. Chen, and M. Bornens, "Cell distribution of stress fibres in response to the geometry of the adhesive environment," *Cell Motility and the Cytoskeleton*, vol. 63, pp. 341–355, June 2006.

[33] J. Lee, A. A. Abdeen, A. S. Kim, and K. A. Kilian, "Influence of Biophysical Parameters on Maintaining the Mesenchymal Stem Cell Phenotype," *ACS Biomaterials Science & Engineering*, vol. 1, pp. 218–226, Apr. 2015.

[34] K. K. Parker, A. L. Brock, C. Brangwynne, R. J. Mannix, N. Wang, E. Ostuni, N. A. Geisse, J. C. Adams, G. M. Whitesides, and D. E. Ingber, "Directional control of lamellipodia extension by constraining cell shape and orienting cell tractional forces," *The FASEB Journal*, vol. 16, pp. 1195–1204, Aug. 2002.

[35] M. Werner, N. A. Kurniawan, and C. V. C. Bouten, "Cellular Geometry Sensing at Different Length Scales and its Implications for Scaffold Design," *Materials*, vol. 13, p. 963, Feb. 2020.

[36] M. Werner, S. B. G. Blanquer, S. P. Haimi, G. Korus, J. W. C. Dunlop, G. N. Duda, D. W. Grijpma, and A. Petersen, "Surface Curvature Differentially Regulates Stem Cell Migration and Differentiation via Altered Attachment Morphology and Nuclear Deformation," *Advanced Science*, vol. 4, p. 1600347, Feb. 2017.

[37] R. W. Style, R. Boltyanskiy, G. K. German, C. Hyland, C. W. MacMinn, A. F. Mertz, L. A. Wilen, Y. Xu, and E. R. Dufresne, "Traction force microscopy in physics and biology," *Soft Matter*, vol. 10, no. 23, p. 4047, 2014.

[38] A. Zancla, P. Mozetic, M. Orsini, G. Forte, and A. Rainer, "A primer to traction force microscopy," *Journal of Biological Chemistry*, vol. 298, p. 101867, May 2022.

[39] A. Denchai, D. Tartarini, and E. Mele, "Cellular Response to Surface Morphology: Electrospinning and Computational Modeling," *Frontiers in Bioengineering and Biotechnology*, vol. 6, p. 155, Oct. 2018.

[40] M. Rodriguez and N. Sniadecki, "Computational modeling of cell mechanics," in *Computational Modelling of Biomechanics and Biotribology in the Musculoskeletal System*, pp. 93–140, Elsevier, 2014.

[41] J. A. Sanz-Herrera, P. Moreo, J. M. García-Aznar, and M. Doblaré, "On the effect of substrate curvature on cell mechanics," *Biomaterials*, vol. 30, pp. 6674–6686, Dec. 2009.

[42] X. He and Y. Jiang, "Substrate curvature regulates cell migration," *Physical Biology*, vol. 14, p. 035006, May 2017.

[43] M. Vassaux and J. L. Milan, "Stem cell mechanical behaviour modelling: substrate's curvature influence during adhesion," *Biomechanics and Modeling in Mechanobiology*, vol. 16, pp. 1295–1308, Aug. 2017.

[44] M. Vassaux, L. Pieuchot, K. Anselme, M. Bigerelle, and J.-L. Milan, "A Biophysical Model for Curvature-Guided Cell Migration," *Biophysical Journal*, vol. 117, pp. 1136–1144, Sept. 2019.

[45] E. Migliorini, E. A. Cavalcanti-Adam, A. E. Uva, M. Fiorentino, M. Gattullo, V. M. Manghisi, L. Vaiani, and A. Boccaccio, "Nanoindentation of mesenchymal stem cells using atomic force microscopy: effect of adhesive cell-substrate structures," *Nanotechnology*, vol. 32, p. 215706, May 2021.

[46] M. Nouri-Goushki, L. Angeloni, K. Modaresifar, M. Minneboo, P. E. Boukany, M. J. Mirzaali, M. K. Ghatkesar, L. E. Fratila-Apachitei, and A. A. Zadpoor, "3D-Printed Submicron Patterns Reveal the Interrelation between Cell Adhesion, Cell Mechanics, and Osteogenesis," *ACS Applied Materials & Interfaces*, vol. 13, pp. 33767–33781, July 2021.

[47] K. Anselme, A. Ponche, and M. Bigerelle, "Relative influence of surface topography and surface chemistry on cell response to bone implant materials. Part 2: Biological aspects," *Proceedings of the Institution of Mechanical Engineers, Part H: Journal of Engineering in Medicine*, vol. 224, pp. 1487–1507, Dec. 2010.

[48] T. M. Svitkina, "Actin Cell Cortex: Structure and Molecular Organization," *Trends in Cell Biology*, vol. 30, pp. 556–565, July 2020.

[49] P. D. Garcia and R. Garcia, "Determination of the viscoelastic properties of a single cell cultured on a rigid support by force microscopy," *Nanoscale*, vol. 10, no. 42, pp. 19799–19809, 2018.

[50] H. Karcher, J. Lammerding, H. Huang, R. T. Lee, R. D. Kamm, and M. R. Kaazempur-Mofrad, "A Three-Dimensional Viscoelastic Model for Cell Deformation with Experimental Verification," *Biophysical Journal*, vol. 85, pp. 3336–3349, Nov. 2003.

[51] M. Ahmad, M. Nakajima, S. Kojima, M. Homma, and T. Fukuda, "Nanoindentation Methods to Measure Viscoelastic Properties of Single Cells Using Sharp, Flat, and Buckling Tips Inside ESEM," *IEEE Transactions on NanoBioscience*, vol. 9, pp. 12–23, Mar. 2010.

[52] M. Li, L. Liu, X. Xiao, N. Xi, and Y. Wang, "Effects of methotrexate on the viscoelastic properties of single cells probed by atomic force microscopy," *Journal of Biological Physics*, vol. 42, pp. 551–569, Oct. 2016.

[53] M. J. Mirzaali, I. C. P. van Dongen, N. Tümer, H. Weinans, S. A. Yavari, and A. A. Zadpoor, "*In-silico* quest for bactericidal but non-cytotoxic nanopatterns," *Nanotechnology*, vol. 29, p. 43LT02, Oct. 2018.

[54] T. D. Nguyen and Y. Gu, "Investigation of Cell-Substrate Adhesion Properties of Living Chondrocyte by Measuring Adhesive Shear Force and Detachment Using AFM and Inverse FEA," *Scientific Reports*, vol. 6, p. 38059, Dec. 2016.

[55] J. G. Mcgarry, J. Klein-Nulend, M. G. Mullender, and P. J. Prendergast, "A comparison of strain and fluid shear stress in stimulating bone cell responses—a computational and experimental study," *The FASEB Journal*, vol. 19, pp. 1–22, Mar. 2005.

[56] E. M. Arruda and M. C. Boyce, "A three-dimensional constitutive model for the large stretch behavior of rubber elastic materials," *Journal of the Mechanics and Physics of Solids*, vol. 41, pp. 389–412, Feb. 1993.

[57] J. S. Milner, M. W. Grol, K. L. Beaucage, S. J. Dixon, and D. W. Holdsworth, "Finite-Element Modeling of Viscoelastic Cells During High-Frequency Cyclic Strain," *Journal of Functional Biomaterials*, vol. 3, pp. 209–224, Mar. 2012.

[58] R. Satcher and C. Dewey, "Theoretical estimates of mechanical properties of the endothelial cell cytoskeleton," *Biophysical Journal*, vol. 71, pp. 109–118, July 1996.

[59] L. Trichet, J. Le Digabel, R. J. Hawkins, S. R. K. Vedula, M. Gupta, C. Ribrault, P. Hersen, R. Voituriez, and B. Ladoux, "Evidence of a large-scale mechanosensing mechanism for cellular adaptation to substrate stiffness," *Proceedings of the National Academy of Sciences*, vol. 109, pp. 6933–6938, May 2012.

[60] S. J. Callens, R. J. Uyttendaele, L. E. Fratila-Apachitei, and A. A. Zadpoor, "Substrate curvature as a cue to guide spatiotemporal cell and tissue organization," *Biomaterials*, vol. 232, p. 119739, Feb. 2020.

[61] F. G. Peet and T. S. Sahota, "Surface Curvature as a Measure of Image Texture," *IEEE Transactions on Pattern Analysis and Machine Intelligence*, vol. PAMI-7, pp. 734–738, Nov. 1985.

[62] J. J. Koenderink and A. J. van Doorn, “Surface Shape and Curvature Scales,” *Image and Vision Computing*, vol. 10, pp. 557–564, Aug. 1992.

[63] A. Gray, “The Gaussian and Mean Curvatures,” in *Modern Differential Geometry of Curves and Surfaces with Mathematica*, pp. 373–380, 481–500, Boca Raton, FL: CRC Press, 2nd ed., 1997.

[64] M. Mercker, *Models, Numerics and Simulations of Deforming Biological Surfaces*. PhD thesis, Universität Heidelberg, Jan. 2012.

[65] X. Sun, K. Wang, H. Wu, J. Chen, and R. Long, “Finite element simulation of a viscoelastic cell entering a cylindrical channel: Effects of frictional contact,” *Mechanics of Materials*, vol. 167, p. 104263, Apr. 2022.

[66] M. N. Dickson, E. I. Liang, L. A. Rodriguez, N. Vollereaux, and A. F. Yee, “Nanopatterned polymer surfaces with bactericidal properties,” *Biointerphases*, vol. 10, p. 021010, June 2015.

[67] J. Hasan, S. Raj, L. Yadav, and K. Chatterjee, “Engineering a nanostructured “super surface” with superhydrophobic and superkilling properties,” *RSC Advances*, vol. 5, no. 56, pp. 44953–44959, 2015.

[68] M. Tanaka, G. Girard, R. Davis, A. Peuto, and N. Bignell, “Recommended table for the density of water between 0 C and 40 C based on recent experimental reports,” *Metrologia*, vol. 38, pp. 301–309, Aug. 2001.

[69] S. Deguchi, T. Ohashi, and M. Sato, “Tensile properties of single stress fibers isolated from cultured vascular smooth muscle cells,” *Journal of Biomechanics*, vol. 39, pp. 2603–2610, Jan. 2006.

[70] W. Ren, L. H. Sneed, Y. Yang, and R. He, “Numerical Simulation of Prestressed Precast Concrete Bridge Deck Panels Using Damage Plasticity Model,” *International Journal of Concrete Structures and Materials*, vol. 9, pp. 45–54, Mar. 2015.

[71] S. D. Guest, “The stiffness of tensegrity structures,” *IMA Journal of Applied Mathematics*, vol. 76, pp. 57–66, Feb. 2011.

[72] T. K. Kim, “Understanding one-way ANOVA using conceptual figures,” *Korean Journal of Anesthesiology*, vol. 70, no. 1, p. 22, 2017.

[73] W. Xi, S. Sonam, T. Beng Saw, B. Ladoux, and C. Teck Lim, “Emergent patterns of collective cell migration under tubular confinement,” *Nature Communications*, vol. 8, p. 1517, Dec. 2017.

[74] J. Wala and S. Das, “Mapping of biomechanical properties of cell lines on altered matrix stiffness using atomic force microscopy,” *Biomechanics and Modeling in Mechanobiology*, vol. 19, pp. 1523–1536, Oct. 2020.

[75] L. Pieuchot, J. Marteau, A. Guignandon, T. Dos Santos, I. Brigaud, P.-F. Chauvy, T. Cloatre, A. Ponche, T. Petithory, P. Rougerie, M. Vassaux, J.-L. Milan, N. Tusamda Wakhloo, A. Spangenberg, M. Bigerelle, and K. Anselme, “Curvotaxis directs cell migration through cell-scale curvature landscapes,” *Nature Communications*, vol. 9, p. 3995, Dec. 2018.

[76] C. M. Bidan, K. P. Kommareddy, M. Rumpler, P. Kollmannsberger, Y. J. M. Bréchet, P. Fratzl, and J. W. C. Dunlop, “How Linear Tension Converts to Curvature: Geometric Control of Bone Tissue Growth,” *PLoS ONE*, vol. 7, p. e36336, May 2012.

[77] P. Oakes, S. Banerjee, M. Marchetti, and M. Gardel, “Geometry Regulates Traction Stresses in Adherent Cells,” *Biophysical Journal*, vol. 107, pp. 825–833, Aug. 2014.

[78] A. Tijore, P. Cai, M. H. Nai, L. Zhuyun, W. Yu, C. Y. Tay, C. T. Lim, X. Chen, and L. P. Tan, “Role of Cytoskeletal Tension in the Induction of Cardiomyogenic Differentiation in Micropatterned Human Mesenchymal Stem Cell,” *Advanced Healthcare Materials*, vol. 4, pp. 1399–1407, June 2015.

[79] C. M. DiGirolamo, D. Stokes, D. Colter, D. G. Phinney, R. Class, and D. J. Prockop, “Propagation and senescence of human marrow stromal cells in culture: a simple colony-forming assay identifies samples with the greatest potential to propagate and differentiate: Human Marrow Stromal Cells in Culture,” *British Journal of Haematology*, vol. 107, pp. 275–281, Nov. 1999.

[80] D. C. Colter, R. Class, C. M. DiGirolamo, and D. J. Prockop, “Rapid expansion of recycling stem cells in cultures of plastic-adherent cells from human bone marrow,” *Proceedings of the National Academy of Sciences*, vol. 97, pp. 3213–3218, Mar. 2000.

[81] D. C. Colter, I. Sekiya, and D. J. Prockop, “Identification of a subpopulation of rapidly self-renewing and multipotential adult stem cells in colonies of human marrow stromal cells,” *Proceedings of the National Academy of Sciences*, vol. 98, pp. 7841–7845, July 2001.

[82] I. Sekiya, B. L. Larson, J. R. Smith, R. Pochampally, J. Cui, and D. J. Prockop, “Expansion of Human Adult Stem Cells from Bone Marrow Stroma: Conditions that Maximize the Yields of Early Progenitors and Evaluate Their Quality,” *STEM CELLS*, vol. 20, pp. 530–541, Nov. 2002.

[83] J. R. Smith, R. Pochampally, A. Perry, S. Hsu, and D. J. Prockop, "Isolation of a Highly Clonogenic and Multipotential Subfraction of Adult Stem Cells from Bone Marrow Stroma," *STEM CELLS*, vol. 22, pp. 823–831, Sept. 2004.

[84] D. Docheva, D. Padula, C. Popov, W. Mutschler, H. Clausen-Schaumann, and M. Schieker, "Researching into the cellular shape, volume and elasticity of mesenchymal stem cells, osteoblasts and osteosarcoma cells by atomic force microscopy," *Journal of Cellular and Molecular Medicine*, vol. 12, pp. 537–552, Apr. 2008.

[85] R. D. González-Cruz, V. C. Fonseca, and E. M. Darling, "Cellular mechanical properties reflect the differentiation potential of adipose-derived mesenchymal stem cells," *Proceedings of the National Academy of Sciences*, vol. 109, June 2012.

[86] A. Shukla, J. H. Slater, J. C. Culver, M. E. Dickinson, and J. L. West, "Biomimetic Surface Patterning Promotes Mesenchymal Stem Cell Differentiation," *ACS Applied Materials & Interfaces*, vol. 8, pp. 21883–21892, Aug. 2016.

[87] M. Versaevel, T. Grevesse, and S. Gabriele, "Spatial coordination between cell and nuclear shape within micropatterned endothelial cells," *Nature Communications*, vol. 3, p. 671, Jan. 2012.

[88] T. Driscoll, B. Cosgrove, S.-J. Heo, Z. Shurden, and R. Mauck, "Cytoskeletal to Nuclear Strain Transfer Regulates YAP Signaling in Mesenchymal Stem Cells," *Biophysical Journal*, vol. 108, pp. 2783–2793, June 2015.

[89] M. Luciano, S.-L. Xue, W. H. De Vos, L. Redondo-Morata, M. Surin, F. Lafont, E. Hannezo, and S. Gabriele, "Cell monolayers sense curvature by exploiting active mechanics and nuclear mechanoadaptation," *Nature Physics*, vol. 17, pp. 1382–1390, Dec. 2021.

[90] D.-H. Kim, B. Li, F. Si, J. Philips, D. Wirtz, and S. X. Sun, "Volume regulation and shape bifurcation in the cell nucleus," *Journal of Cell Science*, p. jcs.166330, Jan. 2015.

[91] M. Versaevel, J.-B. Braquenier, M. Riaz, T. Grevesse, J. Lantoine, and S. Gabriele, "Super-resolution microscopy reveals LINC complex recruitment at nuclear indentation sites," *Scientific Reports*, vol. 4, p. 7362, May 2015.

[92] K. Anselme, P. Davidson, A. Popa, M. Giazzon, M. Liley, and L. Ploux, "The interaction of cells and bacteria with surfaces structured at the nanometre scale," *Acta Biomaterialia*, vol. 6, pp. 3824–3846, Oct. 2010.

[93] D. Leckband and J. Israelachvili, "Intermolecular forces in biology," *Quarterly Reviews of Biophysics*, vol. 34, pp. 105–267, May 2001.

[94] J. P. McGarry, E. O Mairtin, G. Parry, and G. E. Beltz, "Potential-based and non-potential-based cohesive zone formulations under mixed-mode separation and over-closure. Part I: Theoretical analysis," *Journal of the Mechanics and Physics of Solids*, vol. 63, pp. 336–362, Feb. 2014.

[95] E. O. Mairtin, G. Parry, G. E. Beltz, and J. P. McGarry, "Potential-based and non-potential-based cohesive zone formulations under mixed-mode separation and over-closure–Part II: Finite element applications," *Journal of the Mechanics and Physics of Solids*, vol. 63, pp. 363–385, Feb. 2014.

[96] S. T. Wood, B. C. Dean, and D. Dean, "A Computational Approach to Understand Phenotypic Structure and Constitutive Mechanics Relationships of Single Cells," *Annals of Biomedical Engineering*, vol. 41, pp. 630–644, Mar. 2013.

[97] L. Papadakis, E. Karatsis, K. Michalakis, and A. Tsouknidas, "Cellular biomechanics: Fluid-structure interaction or structural simulation?," *Journal of Biomechanics*, vol. 136, p. 111084, May 2022.

[98] Wenxiao Pan, E. Petersen, Ning Cai, Gang Ma, Jian Run Lee, Zhiqin Feng, Kin Liao, and K. Leong, "Viscoelastic Properties of Human Mesenchymal Stem Cells," in *2005 IEEE Engineering in Medicine and Biology 27th Annual Conference*, (Shanghai, China), pp. 4854–4857, IEEE, 2005.

[99] S. C. Tan, W. X. Pan, G. Ma, N. Cai, K. W. Leong, and K. Liao, "Viscoelastic behaviour of human mesenchymal stem cells," *BMC Cell Biology*, vol. 9, p. 40, Dec. 2008.

[100] C.-W. Chang and S. Kumar, "Vinculin tension distributions of individual stress fibers within cell-matrix adhesions," *Journal of Cell Science*, p. jcs.119032, Jan. 2013.

Appendix A

Mesh Convergence and Validation

A mesh convergence and validation study were performed to ensure reliable results. The model was set up as shown in Figure A-1 for both the convergence and the validation studies. The cell was placed on a flat, analytical rigid surface while a rigid sphere (diameter=10µm), signifying the AFM tip, was placed on the apex of the cell. Contact behaviour between the AFM tip and the cell was frictionless, while the contact between the cell and the substrate was the same as in Section 2-3. During the simulation, the AFM tip vertically indented the cell 0.2µm, and the resulting reaction force was recorded.

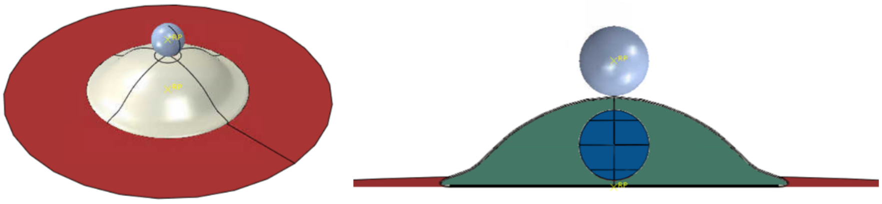

Figure A-1: Model setup for mesh convergence and validation study. Red: flat, analytical rigid surface. White: Actin cortex. Green: CSK. Blue: Nucleus. Grey: AFM tip. Stress fibres are not shown. Left image: isometric view. Right image: Cross-sectional view.

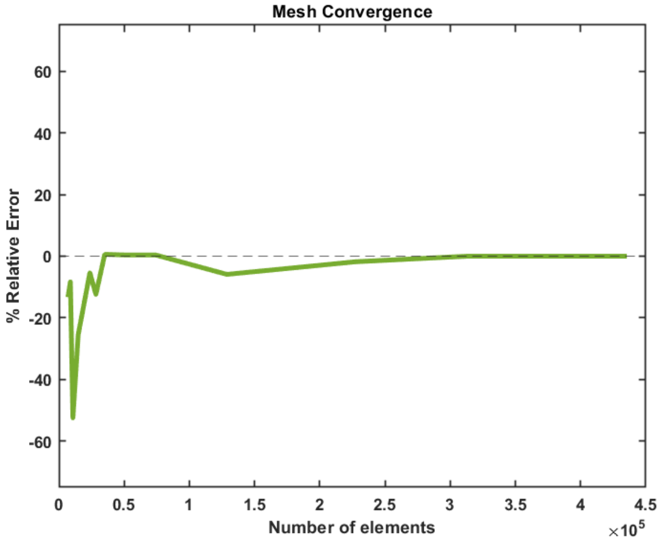

Figure A-2: Mesh convergence study showing the the result converge as the number of elements approaches 300 000.

A-0-1 Mesh Convergence

During the mesh convergence study, the number of elements was increased for each simulation, and the relative error was calculated according to Equation A-1.

$$RelativeError = \frac{RF_n - RF_{n-1}}{RF_{n-1}} \times 100 \tag{A-1}$$

Figure A-2 shows that the model converges as the number of elements approaches 300 000. The details of the final mesh chosen are listed in Table A-1.

Table A-1: Type and number of mesh elements chosen for simulations.

Cellular Components	Element Type	Number of Elements
Actin Cortex	S3	57086
CSK	C3D8H	188 332
Nucleus	C3D8H	11 040
Stress Fibres	T3D2	1202

A-0-2 Validation

The model was validated against experimental results obtained by Migliorini et al. [45]. They used a combination of Matlab/python and FEM to obtain material parameters of the CSK and the actin cortex, listed in Table A-2 and A-3, and obtained force-indentation plots for both in vitro and in silico models. The present model is validated against the in vitro results.

Table A-2: Material parameters derived by Migliorini for ten different hMSC cells using an FEM model excluding adhesive structures.

	Cytoskeleton $\mu_{8\text{chain\_cyto}}$ (Pa)	Cytoskeleton λ_{L_cyto}	Cortex $\mu_{8\text{chain\_cortex}}$ (Pa)	Cortex $\lambda_{L\_\text{cortex}}$	Cytoskeleton $E_{\text{AB\_cyto}}$ (Pa)	Cortex $E_{\text{AB\_cortex}}$ (Pa)
Sample 1	1067.818	3.060	3242.611	3.088	3203.454	9727.833
Sample 2	1656.340	3.070	3201.720	3.085	4969.021	9605.160
Sample 3	1385.048	3.042	3201.467	3.100	4155.143	9604.401
Sample 4	749.359	3.083	3234.576	3.091	2248.076	9703.729
Sample 5	637.246	3.093	3230.370	3.092	1911.739	9691.110
Sample 6	830.987	3.099	3239.491	3.093	2492.962	9718.473
Sample 7	1478.820	3.050	3240.000	3.072	4436.460	9720.000
Sample 8	1446.368	3.027	3241.850	3.068	4339.104	9725.550
Sample 9	916.168	3.094	3194.001	3.097	2748.504	9582.003
Sample 10	802.672	3.092	3214.900	3.091	2408.016	9644.700
Average ± s.d.	1097.083 ± 363.142	3.071 ± 0.025	3224.099 ± 19.149	3.088 ± 0.010	3291.248 ± 1089.426	9672.296 ± 57.447

Table A-3: Material parameters derived by Migliorini for ten different hMSC cells using an FEM model including adhesive structures.

	Cytoskeleton $\mu_{8\text{chain\_cyto}}$ (Pa)	Cytoskeleton λ_{L_cyto}	Cortex $\mu_{8\text{chain\_cortex}}$ (Pa)	Cortex $\lambda_{L\_\text{cortex}}$	Cytoskeleton $E_{\text{AB\_cyto}}$ (Pa)	Cortex $E_{\text{AB\_cortex}}$ (Pa)	E_H (Pa)
Sample 1	1173.014	3.063	3251.228	3.070	3519.041	9753.683	4110.000
Sample 2	1763.387	3.065	3229.130	3.070	5290.161	9687.391	6350.000
Sample 3	1487.424	3.022	3223.649	3.070	4462.273	9670.946	5200.000
Sample 4	858.358	3.070	3245.838	3.085	2575.074	9737.515	3195.000
Sample 5	752.610	3.093	3214.918	3.091	2257.831	9644.755	2800.000
Sample 6	967.037	3.093	3190.000	3.092	2901.112	9570.000	3410.000
Sample 7	1545.920	3.073	3269.109	3.072	4637.760	9807.327	5550.000
Sample 8	1517.130	3.022	3243.060	3.067	4551.390	9729.180	5680.000
Sample 9	1043.050	3.077	3185.068	3.121	3129.150	9555.204	3455.000
Sample 10	880.026	3.075	3205.980	3.087	2640.078	9617.940	3050.000
Average ± s.d.	1198.796 ± 352.630	3.065 ± 0.025	3225.798 ± 27.263	3.083 ± 0.016	3596.387 ± 1057.888	9677.394 ± 81.789	4280.000 ± 1293.194

The model was validated against Sample 3 and Sample 4. For each validation, two simulations were run. First, a simulation without constrained focal adhesions and prestressed actin stress fibres was tested. The second simulation included both constrained focal adhesions and prestressed stress fibres. Figure A-3 shows that Sample 3 correlates better with the experimental results than sample 4. Some differences in behaviour were expected as the present model utilises a slightly different mesh configuration and stress fibre distribution than the model used by Mignorlini to derive the material properties. Moreover, in both cases, the simulations that included the adhesive structures correlated better than the simulations excluding these structures. Finally, the material properties chosen for the study were the average material properties of all ten cells. These parameters were chosen to keep the model as general as possible.

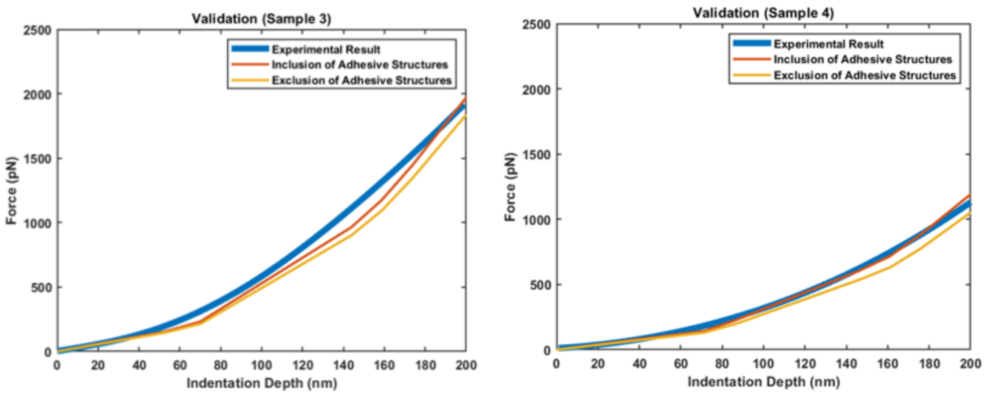
Validation (Sample 3)

Validation (Sample 4)

Figure A-3: Simulations including and excluding adhesive structures compared to experimental results. Left: Sample 3, Right: Sample 4.

Appendix B

Results: SF strain

The contractional force produced an average strain of 0.03 in the SFs, equivalent to an approximate 0.4 µm reduction in length. This constitutes less than 1% of the length of the cell diameter. Consequently, the contractional SF forces have little effect on the overall cell morphology.